


2019

Piezoresistive Behavior of Carbon Nanopaper Polymer Composites for Strain Sensing

Jayden Beyrooti
University of Central Florida

 Part of the [Electro-Mechanical Systems Commons](#)
Find similar works at: <https://stars.library.ucf.edu/etd>
University of Central Florida Libraries <http://library.ucf.edu>

STARS Citation

Beyrooti, Jayden, "Piezoresistive Behavior of Carbon Nanopaper Polymer Composites for Strain Sensing" (2019). *Electronic Theses and Dissertations*. 6748.
<https://stars.library.ucf.edu/etd/6748>

This Masters Thesis (Open Access) is brought to you for free and open access by STARS. It has been accepted for inclusion in Electronic Theses and Dissertations by an authorized administrator of STARS. For more information, please contact lee.dotson@ucf.edu.



PIEZORESISTIVE BEHAVIOR OF CARBON NANOPAPER POLYMER COMPOSITES FOR
STRAIN SENSING

by

JAYDEN BEYROOTI
B.S. University of Central Florida, 2017

A thesis submitted in partial fulfilment of the requirements
for the degree of Master of Science
in the Department of Mechanical and Aerospace Engineering
in the College of Engineering and Computer Science
at the University of Central Florida
Orlando, Florida

Fall Term
2019

Major Professor: Kawai Kwok

© 2019 Jayden Beyrooti

ABSTRACT

Carbon nanopapers made of carbon nanotubes (CNTs) or carbon nanofibers (CNFs), possess unique electrical, thermal and mechanical properties and when integrated with a polymer matrix, can become a multifunctional composite capable of strain sensing and heat actuation. Smart structures such as these can be used in many applications including deployable space structures, human motion detection, and structural health monitoring as flexible, sensitive and stable strain sensors in addition to providing electrical heat actuation for the shape memory effect in polymers. This study focuses on strain sensing capabilities by developing a numerical model to predict piezoresistive behavior. The piezoresistive effect is a change in resistivity of a conductive network when a deformation is applied. This allows strain to be determined by simply measuring the electrical resistance. An equivalent resistor network can be formed to represent the fiber network. The proposed 2D model generates randomly oriented fibers inside a unit cell, determines their intersection points, and creates a mesh of the network for finite element analysis. Electrical conductivity is found for the initial and deformed fiber states by determining the current through the network for a known voltage. A piezoresistivity experimental study is conducted to investigate the strain sensing abilities of this material and validate model results. This simple model provides an initial framework that can be developed in future work. Despite its 2D nature, the model captures the governing mechanisms of piezoresistivity to a certain extent.

For my brother, Seth

ACKNOWLEDGMENTS

I am very grateful to my advisor, Dr. Kawai Kwok, for being an excellent mentor and so supportive throughout my studies. Thank you for guiding me in my research endeavors. I have learned much under your instruction. I will keep in mind the many pieces of advice you have given me and will apply the knowledge gained in this experience to future ventures.

I also gratefully acknowledge Dr. Jeffrey Kauffman and Dr. Jihua Gou for being on my committee and for advising me throughout all stages of my study.

My labmates and good friends have been incredibly supportive and have made the time during my study very enjoyable. I offer many thanks to my labmates Veli Bugra Ozdemir, Milinda Yapa Hamillage, Wolfgang Klimm, Andrew Gomez-Delrio and Dr. Alejandro Carrasco-Pena. I also thank my friend Xiangpeng Li for his support. I especially recognize Veli and Wolfgang for their help in writing the model code.

A special thanks goes to the NASA Florida Space Grant Consortium for supporting this study. I am very appreciative for the opportunity to have worked on this research.

Last but not least, I thank all of my family but especially my Mom and Dad for their love and encouragement.

TABLE OF CONTENTS

LIST OF FIGURES	ix
LIST OF TABLES	xii
CHAPTER 1: INTRODUCTION	1
1.1 Carbon Nanopaper	1
1.2 Motivation	3
1.3 Objectives	6
CHAPTER 2: LITERATURE REVIEW	7
2.1 Carbon Nanomaterial Based Strain Sensors	7
2.2 Carbon Nanomaterial Piezoresistivity Models	9
2.2.1 Piezoresistive Effect	9
2.2.2 Tunneling Effect	10
2.2.3 Percolation Theory	13
2.2.4 Electrical Conductivity Models	15
2.2.5 Strain Sensitivity	18

CHAPTER 3: MATERIALS AND COMPOSITE FABRICATION	19
3.1 Materials Selection	19
3.1.1 Carbon Nanopaper	20
3.1.2 Polymer Matrix	23
3.2 Composite Fabrication	23
CHAPTER 4: PIEZORESISTIVITY EXPERIMENTAL STUDY	25
4.1 Materials Characterization	25
4.1.1 Four Point Probe Resistivity Measurements	25
4.1.2 Electromechanical Tests	29
4.2 Carbon Nanopaper Piezoresistive Characterization	31
4.3 Composite Piezoresistive Characterization	34
CHAPTER 5: MODEL DEVELOPMENT AND IMPLEMENTATION	40
5.1 Model Construction	40
5.1.1 Microstructure Generation	41
5.1.2 Fiber Intersection	43
5.1.3 Mesh Generation	44
5.1.4 Equivalent Resistor Network Formation	46

5.1.5	Electrical Conductivity Determination	48
5.1.6	Deformation of the Microstructure	49
5.2	Sensitivity Study of Input Parameters	52
5.2.1	Fiber Dimensions and Concentration	53
5.2.2	Tunneling Parameters	58
5.2.3	Voltage Variations	61
5.3	Model Results	63
CHAPTER 6: RESULTS DISCUSSION		67
6.1	Experimental and Model Results Comparison	67
6.2	Model Limitations	68
CHAPTER 7: CONCLUSION		70
7.1	Findings	70
7.2	Future Work	70
APPENDIX A: MATLAB CODE		73
APPENDIX B: ABAQUS INPUT FILE		87
LIST OF REFERENCES		93

LIST OF FIGURES

1.1	Applications: Deployable Space Structures, Human Motion Detection , Adaptive Aircraft Structures, Structural Health Monitoring	3
2.1	Tunneling Conductivity at a Junction	13
2.2	Percolation Behavior of Conductive Networks	14
3.1	Carbon Nanopaper SEM Images	22
3.2	Composite Mold	24
4.1	Carbon Nanopaper Sample and Square Grid Pattern	27
4.2	Signatone Quad Pro System	28
4.3	Composite Four Wire Measurement	29
4.4	Electromechanical Tests Experimental Setup	30
4.5	Carbon Nanopaper Fracture Pattern	31
4.6	Carbon Nanopaper Fracture Test Results	32
4.7	Carbon Nanopaper Experimental Setup	33
4.8	Carbon Nanopaper Stretch Results 0.4% Strain	33
4.9	Composite Experimental Setup	34

4.10	Stretch Results 2% Strain	36
4.11	Stretch/Release Results 2% Strain	37
4.12	3 Cycle Results 2% Strain	38
4.13	15 Cycle Results 2% Strain	39
5.1	2D Fiber Generation	42
5.2	Fiber Intersection	44
5.3	Fiber Network Mesh	45
5.4	Circuit Representation of Fiber Network	47
5.5	Current Summation at Source Electrode	49
5.6	Deformed Fiber Network	51
5.7	Percolation Voltage Contours for Increasing Number of Fibers	54
5.8	Percolation Behavior of Fiber Network	55
5.9	Conductivity Changes for Varying Fiber Diameters	56
5.10	Voltage Contours for Increasing Fiber Lengths	57
5.11	Conductivity Changes for Varying Fiber Lengths	58
5.12	Conductivity Changes for Varying Energy Barrier Heights	59
5.13	Number of Junctions Histogram	60

5.14	Composite Conductivity Changes for Varying Tunneling Shells	61
5.15	Voltage Variations	62
5.16	Current Density and Voltage Contours for Initial Network State	64
5.17	Piezoresistive Current Density and Voltage Contours at 2% Strain	65
6.1	Model and Experimental Results Comparison	68
7.1	3D Fiber Network	71

LIST OF TABLES

2.1	Physical Constants	11
2.2	Energy Barrier Heights for Various Polymers	11
3.1	Carbon Nanofiber Material Properties	20
3.2	Carbon Nanopaper Material Properties	21
3.3	Silicone Rubber Material Properties	23
4.1	Carbon Nanopaper Four Point Probe Results	28
4.2	Carbon Nanocomposite Four Point Probe Results	29
4.3	Composite Material Properties	35
5.1	Material Properties Input Parameters	41
5.2	Simulation Input Parameters	63
5.3	Model Conductivity and Piezoresistivity Results	66
6.1	Model and Experimental Results Comparison	67

CHAPTER 1: INTRODUCTION

1.1 Carbon Nanopaper

Carbon nanopaper is a thin film made of carbon nanofibers (CNFs) or carbon nanotubes (CNTs). Carbon nanotubes can be single walled (SWCNTs) or multiwalled (MWCNTs). SWCNTs have diameters ranging from 0.6 - 0.8 nm while MWCNTs have diameters ranging from 5 - 50 nm. Both have aspect ratios from 100 - 10000, thermal conductivities from 3000 - 6000 W/mK, and a resistivity as low as $0.001 \Omega \text{ cm}$ [1]. Since CNTs have small diameters with very high aspect ratios, they are more affected by Van der Waals forces, causing the nanotubes to reassemble and requiring the need of chemical dispersants to maintain an adequate dispersion. This makes it difficult to evenly disperse CNTs in a polymer matrix and results in agglomerations which in turn can adversely affect electrical properties [2].

CNFs experience weaker Van der Waals forces and maintain their original dispersion for longer periods of time. Vapor grown carbon nanofibers are produced in a manner similar to carbon black. The nanofibers are manufactured by pyrolysis of a hydrocarbon feedstock like natural gas, or carbon monoxide on a metal catalyst like iron. This is a good process for mass production as it is inexpensive and produces well defined diameters. CNFs have diameters ranging from 50 - 200 nm, aspect ratios from 250 - 2000, a thermal conductivity of 1950 W/mK, and a resistivity as low as $0.0001 \Omega \text{ cm}$ [1].

Carbon nanomaterials (CNMs) manufactured in nanopaper form, have the benefit of the fibers being relatively evenly distributed in the matrix with minimal agglomeration. Nanopapers made of CNTs are typically referred to as buckypaper. Carbon nanopapers are made up of self-supporting, random networks of entangled CNTs or CNFs and are held together by van der Waals forces at the

junctions [3]. Fiber networks are deposited on a substrate using a surfactant which is then evaporated. Alternatively, an ink made of the CNMs can be 3D printed to create layers of a nanopaper. The conductive network formed by these nanomaterials allows the piezoresistive effect to occur, which is the change in electrical resistance when the network undergoes a deformation. This allows for accurate, stable, linear and repeatable strain sensing capabilities of a carbon nanopaper/polymer composite due to its good piezoresistive behavior. Not only does nanopaper greatly improve mechanical properties of a polymer matrix composite, it also provides excellent electrical and thermal properties. CNFs have an extremely high heat transfer rate making them excellent candidates for Joule heating applications. A voltage applied to the nanofibers heats them to high temperatures which in turn heats the surrounding polymer matrix beyond the glass transition temperature, thus initiating the shape memory effect. For these reasons, carbon nanopaper made of CNFs was selected as the conductive filler for this study. The model developed in this study is applicable to all carbon nanomaterials (i.e. nanotubes and nanofibers). Throughout this work, the conductive filler is referred to as fibers.

1.2 Motivation

Carbon nanopapers possess unique electrical, thermal and mechanical properties and when integrated with a polymer matrix, can become a multifunctional composite capable of strain sensing and heat actuation. Smart structures such as these can be used in the applications displayed in Figure 1.1, including deployable space structures [4], human motion detection [5], adaptive aircraft structures [6] and structural health monitoring [7]. These multifunctional composites are used as flexible, sensitive and stable strain sensors in addition to providing electrical heat actuation for the shape memory effect in polymers.



Figure 1.1: Applications: Deployable Space Structures, Human Motion Detection , Adaptive Aircraft Structures, Structural Health Monitoring

High altitude balloons can greatly benefit from the high strain capabilities and flexibility of the nanocomposite. Deployable structures can greatly benefit from the shape memory effect of polymers; the ability to store a programmed shape and recover to an initial shape when stimulated by heat, light, electricity or magnetism. Conductive and thermally stable fillers can provide Joule heating to initiate the shape recovery. Carbon nanopaper/shape memory polymer composites can use closed loop control to actively manage shape recovery behavior [8]. Carbon nanopaper has been shown to significantly improve electrical conductivity, allowing for fast actuation and lower input voltages [9, 10, 11, 12].

Smart aircraft skins can also be developed with these materials. Geometries that have very thin regions, like leading edges, or sharp changes, like the wing/fuselage junction, are difficult areas to monitor with an instrument. A structural health monitoring sensor can measure strain, temperature and pressure within the structure and at the structure surface. Like the deployable structures applications, the sensor can be used as an actuator for adaptive aircraft wings. They offer a structurally efficient and repeatable way of deflecting a portion of a wing while in flight. This provides a better aerodynamic efficiency, since the motion of the rudder can be reduced to control yaw [6]. Additionally, composites made of this material are excellent at damping vibrations in aircraft structures [13]. Furthermore, carbon nanopaper based composites are promising candidates for aircraft electromagnetic interference shielding, fire protection and lightning strike protection [14].

This material not only benefits aerospace structures, but also biomedical engineering [15]. Carbon filled elastomeric materials can be used as sensors for human motion detection, artificial skin and wearable medical devices. Wearable electronics made of carbon nanomaterial based polymer composites exhibit excellent flexibility, conformability to complex geometry like the human body, and are lightweight and soft. Wang et al. [16] studied highly stretchable and wearable CNT printed strain sensors to monitor complex human motions. The sensors are wearable and highly accurate for multidirectional strain. Kim et al. developed stretchable circuits that are not only cost

effective but stable and have been used for biopotential measurements such as electrocardiograms, electroencephalograms and electromyograms [17].

Flexible skins capable of tactile imaging and strain sensing are beneficial to both biomedical applications and robotic grappling mechanisms. These skins are compliant enough to determine contact. Some studies have employed electrical impedance tomography to image internal conductivity distribution, ensuring sensitivity throughout the whole sensor [18]. By using a spray deposition modeling printing process, CNT layers can be adjusted to alter sensing properties. Suzuki et al. [5] incorporated unidirectionally aligned multiwalled CNTs between elastomer layers to create a lightweight, wearable sensor capable of rapid response of body motions. They worked with Yamaha to use this device to monitor a pianist's hands during play. Wang et al. [19] fabricated strain sensors with a high gauge factor capable of detecting a full range of human motions such as finger and wrist bending, artery pulses and laryngeal prominence. De Graff et al. similarly developed glove sensors out of ultra-thin buckypapers that are capable of detecting microstrains with good linearity in extension and compression [20]. Not only does this allow for easy calibration, but also excellent repeatability. Ultra-thin buckypapers are printable, low-profile and affordable. However, some issues need to be overcome before commercial devices can be manufactured; such as, nonlinearity, hysteresis, cycling repeatability and an undesired viscoelastic response [21].

Carbon nanomaterial based sensors can be embedded in structures of various geometries and can continuously monitor conditions both inside and on the structure surface. The ability to align nanotubes into specific orientations make these sensors particularly effective for structural health monitoring applications. NASA's Langley Research Center has developed a dense, highly ordered array of CNTs that is not only flexible but capable of crack growth detection and strain field mapping [7]. When a filler network is damaged, the corresponding region experiences a loss in conductivity which can allow for self-sensing. Electrical impedance tomography can continuously and non-invasively image the internal conductivities of a structure, allowing for the determination

of displacements, stresses and strains [22]. Dang et al. [23] developed a high elasticity nanocomposite capable of compression stress monitoring. One civil engineering application includes in situ compressive strain monitoring of displacements on foundations for a new building [24]. These sensors were easy to setup on site and successfully monitored strain during each construction phase. Additionally, these sensors can be embedded in roads, bridges and tunnels.

It can be seen that these multi-functional composites have the potential to be effective strain sensors and actuators. However, carbon nanopaper microstructure is extremely complex and the electron transport behavior in the fiber network and corresponding piezoresistive behavior is not well understood. There are also several uncertainties associated with predicting the electrical conductivity of randomly clustered fiber networks. Several current predictive numerical models are very complex and computationally expensive.

1.3 Objectives

The primary objective of this study is to develop and implement a simple 2D model relating the coupled electromechanical response of carbon nanofiber networks. The electrical conductivity and piezoresistivity of the network are to be predicted through numerical simulation. Model performance will be assessed by a sensitivity study of varying input parameters. This model will allow for the design of strain sensors without the need of fabrication. Experimental tests are conducted to validate this concept. A composite with good bonding between the fibers and matrix will be fabricated, and a piezoresistivity study conducted to assess strain sensing characteristics. This model will provide an initial framework that can be later developed by considering several new factors that will improve model accuracy and be applicable to more material designs.

CHAPTER 2: LITERATURE REVIEW

2.1 Carbon Nanomaterial Based Strain Sensors

While conventional metallic strain gauges are less expensive and have high sensitivities at high strains, they have several limitations. These include lack of flexibility, poor sensitivity at low strain, unidirectional strain restrictions and they cannot be embedded in structural materials [25]. Fiber Bragg Grating (FBG) sensors are capable of measuring very high strains, can be embedded into structures and are well suited for composite design. However, they have poor strain resolution on the nanoscale. Carbon nanomaterial thin film polymer composites are capable of multidirectional, high strain resolution on the nanoscale, can be embedded in structural materials, and have unique multifunctional capabilities due to their excellent electrical properties. CNM architecture for strain sensing has been researched in recent years including pure CNT yarns and buckypaper, hybrid composites with aligned or random nanotube dispersions, nanofibers and bulk composites [26, 27].

CNT thin films are made up of randomly oriented single (SWCNTs) or multiwalled carbon nanotubes (MWCNTs), resulting in electrical properties independent of direction. Obitayo and Liu [28] concluded that small gap semiconducting single-walled CNTs have the greatest sensitivity of CNT films. However, MWCNTs exhibit a more metallic nature than SWCNTs in regards to electrical conductivity and typically create a more conductive composite [29]. Li et al. [26] found that applying a pre-straining process improves piezoresistive performance, producing a closer to linear behavior over wider strain ranges. Vermuru et al. [30] studied real time voltage changes as a function of temperature for MWCNT macroscale strain sensors. Rein et al.[31] investigated the coupling between mechanical and electrical properties of embedded buckypaper strain sensors and concluded that they are sensitive to the geometry of local defects. As discussed in the aforementioned human motion detection application, certain CNM composites are capable of high

deformations. Zhu et al. [32] found resistivity to have a reversible response up to 120% strain.

Composites containing various types of fillers have also been studied. Natarajan et al. [33] found for natural rubber composites that CNTs showed strong strain response in the 100% to 150% strain regime while carbon black showed good strain response in the 50% to 100% strain regime. By combining these two fillers, their respective properties could be exploited, and a sensor tailored to have a responsive operating regime from 50% to 150% strain. Other studies have used blends of carbon nanopaper and electromagnetic CNTs to greatly improve electromagnetic behavior [34].

While composites fabricated by mixing CNTs and dispersing them in a solution has shown to produce adequate strain sensors, certain advantages exist for using nanopaper forms of fillers rather than dispersed particles. Particles are not always dispersed evenly, resulting in agglomerates. A high concentration and even dispersion are needed to create a percolating network. Carbon nanopaper is manufactured with a relatively even dispersion and minimal agglomerates. Additionally, it bonds well with polymers which is essential for strain sensing applications. Multi-layered papers have greatly improved conductivity and temperature distribution for these composites [35]. Buckypapers, films made of CNTs, are frequently used. These nanopapers are also capable of multi-directional strain sensing [36]. Thin film type transistors also possess a similar electron transport behavior and have been studied using 2D percolating networks of both tubes and wires [37, 38]. Metallic strain gauges have gauge factors up to 5 while carbon nanopaper based strain sensors have gauge factors up to 80.

2.2 Carbon Nanomaterial Piezoresistivity Models

The governing mechanisms of piezoresistivity and current electrical conductivity models associated with carbon nanomaterial based strain sensors are now presented.

2.2.1 Piezoresistive Effect

The piezoresistive effect is a change in resistivity of a conductive network when a strain is applied. The basis of piezoresistivity is in the dependence of conductivity of fiber networks through which electrons travel by tunneling through thin insulating barriers. Conductivity is greatly dependent on the distance between fibers. When the network experiences a mechanical influence such as a force or strain, fiber positions and orientations change. This results in a change in electrical resistance which can be measured by a multimeter.

Resistivity (ρ) can be expressed as the following where R is resistance, A is cross-sectional area, and L is length.

$$\rho = R \frac{A}{L} \quad (2.1)$$

Conductivity (σ) is simply the inverse of resistivity.

$$\sigma = \frac{1}{\rho} \quad (2.2)$$

The piezoresistive effect allows CNM composites to be used as strain sensors by simply measuring the electrical resistance during deformation. The basis of piezoresistive properties of CNT thin films is due to changes in the band gap when under strain [28]. Resistivity changes due to deformation can be attributed to the change in network configuration and the deformation of the fibers themselves [39].

2.2.2 Tunneling Effect

Three types of resistances exist in a percolating network of fibers; the intrinsic resistance of the fibers, the contact resistance between intersecting fibers, and the tunneling resistance between two fibers that are very close to each other but not touching. If two electrodes are separated by a sufficiently thin insulating barrier, it is possible for electrons to jump the gap, thus allowing current to flow. This is known as the tunneling effect. Individual fibers have a very low intrinsic resistance. Contact resistance, while higher than the intrinsic, is still significantly low. However, during fabrication, the polymer matrix tends to encapsulate most fibers with a very thin insulating layer. This prevents fibers from being in direct contact with each other. Furthermore, Van der Waals forces tend to prevent contact between carbon particles [40]. The tunnelling resistance is the dominant resistance of the three and as such, the other two are neglected in this study [41]. Research has been done that incorporates these values but since the tunneling resistance is several orders of magnitude higher than the other two, most studies consider them negligible. Hu et al. [42] concluded that the tunneling effect is mainly responsible for affecting the piezoresistive response of CNT-polymer composites.

The following equation derived by Simmons [43] is used to calculate the tunneling resistance of a junction.

$$R_{tun} = \frac{V}{AJ} = \frac{h^2 t}{A q_e^2 \sqrt{2 m_e \lambda}} \exp\left(\frac{4\pi}{h} \sqrt{2 m_e \lambda} t\right) \quad (2.3)$$

V is the electric potential difference, J is the current density, A is the cross-sectional area of the tunnel, h is Planck's constant, λ is the energy barrier height, q_e is the elementary charge, m_e is the mass of an electron and t is the insulator thickness. The values for the physical constants are displayed in Table 2.1. The energy barrier height of the matrix is in units of electronvolts. One electronvolt is equivalent to 1 J/C or when multiplied by the elementary charge, 1.602×10^{-19} J.

Table 2.1: Physical Constants

Measure	Value	Unit
Planck's Constant	6.626×10^{-34}	$m^2 \cdot kg/s$
Electron Mass	9.10938×10^{-31}	kg
Electron Charge	1.602×10^{-19}	C

The insulator thickness, or tunneling shell, can be calculated for given fiber and matrix properties. It can be regarded as the minimum distance where electrons can jump between fibers. The tunneling shell is typically less than 2 nm for carbon nanomaterials. Slight strains are capable of being measured because the equivalent resistance of a tunneling junction is exponentially dependent on the length of the tunneling shell. The tunneling shell is estimated in this model based off values found in literature and verified experimentally by measuring the resistivity of the undeformed composite. The tunneling shell is dependent on the following properties: fiber length, fiber volume fraction, initial composite resistivity and the energy barrier height of the matrix.

As seen by the tunneling equation, the energy barrier height significantly influences electrical conductivity of the composite, especially at lower filler volume fractions [44]. Table 2.2 displays some typical values for λ [45, 46, 47, 48]. It ranges from 0.5 to 5 eV for most polymers. It is the only matrix property that influences tunneling in this model.

Table 2.2: Energy Barrier Heights for Various Polymers

Polymer	λ (eV)
Polydimethylsiloxane	0.73 - 1
Epoxy	0.50 - 2.50
Silicone Rubber	3.3 - 3.8
Silicon	4.05
Polystyrene	4.22
Polytetrafluoroethylene	4.26
Polycarbonate	4.26
Epoxy Resin	5.00

Ruschau [49] developed a model to determine the number of conductive pathways, N , that exists between the source and drain electrodes and the number of fibers, M , that comprise these pathways. The tunnelling equation by Simmons [43] is first rearranged to represent resistivity. Overall conductivity of the unit cell can be determined by multiplying the individual resistivity by the ratio of number of conducting fibers to conductive pathways.

$$\rho_{tun} = \frac{M}{N} \frac{h^2}{q_e^2 \sqrt{2m_e \lambda}} \exp\left(\frac{4\pi}{h} \sqrt{2m_e \lambda} t_0\right) \quad (2.4)$$

This equation can be modified to represent fiber length and volume fraction instead of number of pathways and number of fibers. A tunneling vector can be defined as a line segment connecting two fibers in the direction of the tunneling effect. The initial tunneling vector, t_0 , can be found by solving the tunneling resistance equation when it takes fiber volume fraction and fiber length into account [50]. This is only for the composite in an undeformed state.

$$R_0 = \frac{\pi^5 h^2 t_0}{64 v_f l_{CNF} q_e^2 \sqrt{2m_e \lambda}} \exp\left(\frac{4\pi}{h} \sqrt{2m_e \lambda} t_0\right) \quad (2.5)$$

Since the desired variable, t_0 , exists both inside and outside of the exponent of the tunneling equation, the Lambert function, $W(z)$, can be used to solve for it. It provides solutions for any complex number, z .

$$z = f^{-1}(ze^z) = W(ze^z) \quad (2.6)$$

Once the Lambert function is used to solve the tunneling equation, the tunneling shell can be expressed as,

$$t_0 = \frac{h}{4\pi \sqrt{2m_e \lambda}} W\left(\frac{2^9 q_e^2 l_{CNF} m_e v_f \rho_0 \lambda}{h^3 \pi^4}\right) \quad (2.7)$$

This equation provides the initial thickness of the insulating polymer or the minimum distance between fibers in which tunneling will occur. Figure 2.1 illustrates how much the tunneling shell and

the energy barrier height affect conductivity. Conductivity can change several orders of magnitude depending on fiber proximity.

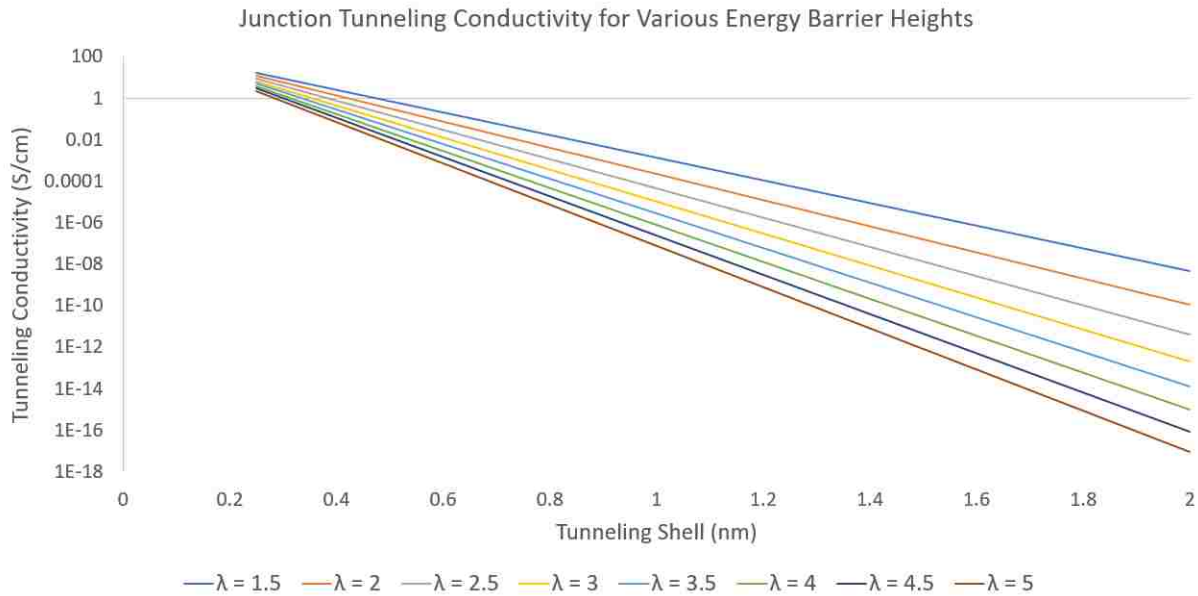


Figure 2.1: Tunneling Conductivity at a Junction

This model assumes that any fibers in contact will have a resistivity as defined by the tunneling equation since the insulator thickness is significantly smaller than fiber diameter and tunneling is the dominant form of resistance. The intrinsic resistance of individual fibers is several orders of magnitude smaller and is therefore neglected.

2.2.3 Percolation Theory

The formation of conductive networks of carbon nanomaterials obeys percolation theory which describes the phase transition of randomly connected clusters [51]. Kirkpatrick [52] originally described the insulator to conductor phase transition of conductive particle based composites using percolation theory. There exists a percolation threshold where a certain filler density results in a

significant increase in conductance. Studies have shown that a higher strain sensitivity can be achieved when the conductive filler is at the percolation threshold [42]. Electrical conductivity of the composite is significantly higher at or above the percolation threshold. As conductivity is dependent on the number of fibers, three cases exist that are of interest. State 1 is insulating, State 2 is the percolation threshold and State 3 is highly conductive, as shown in Figure 2.2.

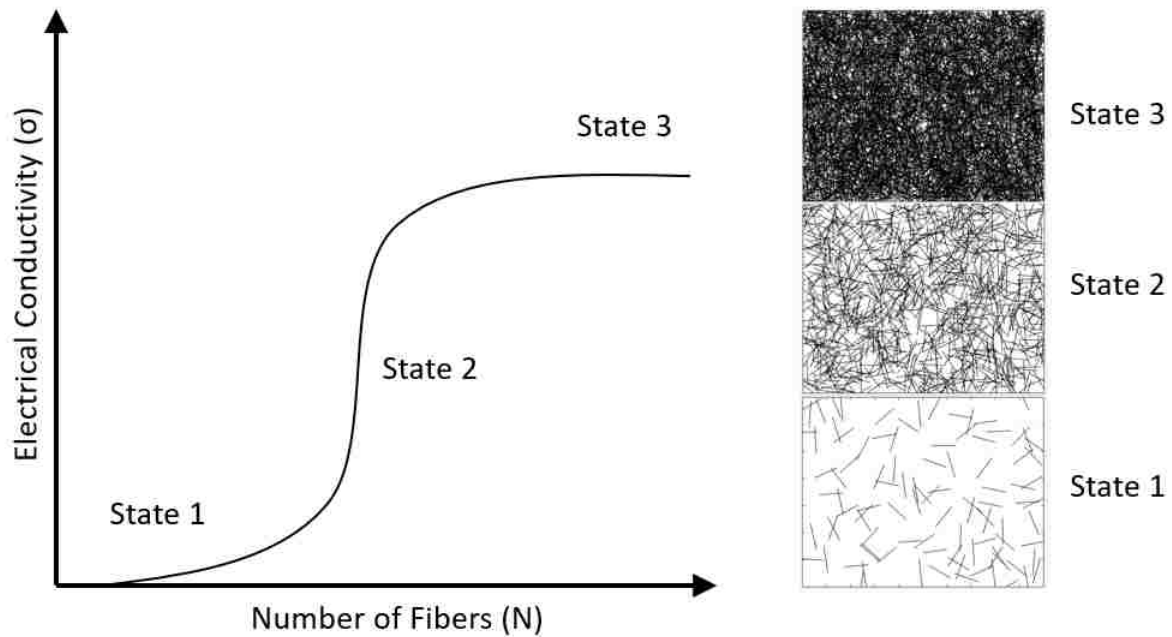


Figure 2.2: Percolation Behavior of Conductive Networks

Inhomogeneous spatial distribution of CNTs or CNFs by traditional composite manufacturing techniques can result from inadequate distribution during the mixing process. Carbon nanopapers ensure that a percolating network exists between two electrodes. In a representative volume element, conductive pathways between two electrodes are formed at or above the percolation threshold. Percolation probability (P) is the probability that at least one conductive path exists between the source and drain electrodes of a unit cell. It is simply the ratio of cases where conductive paths

exist (n_p) to total number of simulations (n_t).

$$P = \frac{n_p}{n_t} \quad (2.8)$$

Studies have shown that several factors affect the percolation threshold and conductivity; namely, polymer type, CNM aspect ratio, dispersion degree and agglomerate disentanglement [53, 54]. Of these factors, filler aspect ratio has the greatest effect on the percolation threshold [55]. With increasing filler concentration, the shortest distance between fibers decreases due to the Van der Waals interaction [40]. The shorter tunneling shell results in a much more conductive network. A scaling law is used to describe conductivity above the percolation threshold.

$$\sigma = \sigma_0(\phi - \phi_c)^t \quad (2.9)$$

ϕ is the weight fraction of the conducting filler, ϕ_c corresponds to the percolation threshold and t is the critical exponent. The critical exponent only depends on system dimensionality; $t = 1.6$ for 2D and $t = 2$ for 3D [53]. Aligned CNMs can also lower the percolation threshold [26].

2.2.4 Electrical Conductivity Models

Several properties influence the electrical conductivity of polymer composites; such as, filler size, distribution, aspect ratio, matrix and filler interaction, surface energy and processing techniques. Therefore, much study has been done on models to predict electrical conductivity. Three main types of models exist; equivalent resistor network models, computational micromechanics models, and analytical models.

Equivalent resistor network models discretize the fibers and tunneling junctions into resistor elements. Conductivity is determined by solving the electrical circuit. Resistor network models are

common because they can accurately capture geometric complexities of typical fiber networks. However, they can be computationally expensive due to the high number of fibers involved. Yasuoka et al. [51] developed an electrical circuit simulation to determine piezoresistivity where each fiber is modeled as a resistor. Kumar et al. [38] assumed junction resistance as a constant. Behnam and Ural [56] developed a resistor network that is solved by Kirchhoff's current law in terms of conductance. Hu et al. [57] considered the change of the internal conductive network, fiber's piezoresistivity and the tunneling effect all in one 3D resistor network model.

Computational micromechanics models consider both the fibers and the surrounding matrix by the finite element method. While these models can incorporate mechanical effects such as fiber/matrix debonding, they do not accurately capture the geometric complexities of a fiber network [22]. Oliva-Aviles et al. [39] correlated macroscale composite strain to individual CNT strain by a micromechanics model. Bao et al. [58] showed that electron tunneling effects are more pronounced in SWCNTs composites than MWCNTs. Additionally, they showed that CNT contact resistance represented by the Landauer-Buttiker formula accounts for both tunneling and contact resistances [58]. Ren and Seidel [59] developed an electromechanically coupled code to assess in-plane and axial piezoresistive responses of CNT/polymer composites.

Analytical models derive explicit functions of filler parameters without directly modeling the fibers [60]. Assumptions have to be made regarding fiber distribution and orientation which may result in some local inaccuracies. The General Effective Media (GEM) model is frequently used because it is capable for multiple filler types and it calculates a conductivity value above the percolation threshold [61]. Zare and Rhee [62] developed a simple methodology to predict tunneling conductivity by considering CNT waviness and interphase thickness and their effect on percolation threshold and effective filler concentration. Wang and Zhao [63] developed a simple analytical model to predict both electrical conductivity and piezoresistivity by considering electron jumping and conductive networks without resorting to heavy computation. Panozzo et al. [50] analytically

estimated piezoresistive behavior while accounting for random fiber orientations, waviness and entanglements.

The resistor network model was selected for this study to represent the random microstructure of the fiber network. A unique approach was taken to minimize computation time by creating a microstructure and solving for conductivity by electrical circuit simulation. The conductive fiber network can be represented as resistors in parallel. Current can be solved by Kirchhoff's Current Law; the sum of currents flowing into a junction (n) is equal to the sum of currents (I) flowing out of a junction.

$$\sum_{k=1}^n I_k = 0 \quad (2.10)$$

The current law is used in conjunction with Ohm's Law to solve for the current passing through a circuit of known potential.

$$I = V/R \quad , \quad J = \sigma E \quad (2.11)$$

V is voltage, R is resistance, J is current density and E is electric field.

As discussed, the percolation based approach for this study is a probabilistic method and as such, Monte Carlo simulations are typically conducted to obtain numerical results for repeated random samplings. Since fibers are generated with random positions and orientations, several runs are made to ensure an accurate result. Results are typically presented as a histogram to analyze the distribution. Monte Carlo simulations have also been employed to determine geometry dependent resistivity scaling based on parameters like fiber density, length and alignment [56].

2.2.5 Strain Sensitivity

Sensors need to exhibit good stability and repeatability. The gauge factor (GF) is calculated to represent the sensitivity of the strain sensors. It is simply the ratio of changes in electrical resistance ($\Delta R/R_0$) and the applied strain (ϵ). The repeatability error, or standard deviation, of the gauge factor can be used to determine the coefficient of variation, which is a measure of the degree of data dispersion. A strain sensor with good stability will have a small coefficient of variation. It is expected that electrical resistance will increase almost linearly with strain and the gauge factor will remain almost constant. Strain sensitivity is best observed by plotting relative resistance change by strain. The gauge factor is the slope of this plot and an excellent indicator of strain sensitivity.

$$\frac{\Delta R(\epsilon)}{R_0} = \frac{R(\epsilon)}{R_0} - 1 \quad (2.12)$$

$$GF = \frac{\Delta R/R_0}{\epsilon} \quad (2.13)$$

A critical strain exists in which piezoresistive behavior is rendered irrecoverable. Below the critical strain, fiber networks break and return close to their original positions, producing a repeatable piezoresistive response. Beyond the critical strain, conductive networks experience permanent deformation resulting in damaged networks that cannot return to their original conductivities. It is imperative that the strain sensors operate below the critical strain. Matrix mechanical behavior is therefore another significant design parameter as yielding and plastic deformation can result in irreversible resistance changes [64].

CHAPTER 3: MATERIALS AND COMPOSITE FABRICATION

3.1 Materials Selection

Interfacial bonding is a governing mechanism for electron and stress transfers [65]. The interfacial bonding strength between fillers and matrix depends on CNF or CNT type. Polymer composites containing dispersed fibers are common but pose some disadvantages. Powders of CNFs or CNTs are mixed in a solvent with sonication to attempt an even distribution. However, it is difficult to evenly disperse particles in the matrix and this results in agglomerates and the possibility that percolation may not take place. Nanopapers are manufactured by taking CNFs or CNTs and forming them as thin films with a solvent. The solvent is then evaporated producing a relatively even network distribution. Since the formation of agglomerates is minimal and percolation is guaranteed, nanopapers were selected for this study. The model best represents nanopapers as it does not consider agglomerations. Sheets of nanofibers were selected for this study because they can be more conductive at lower volume fractions simply because they are bigger than nanotubes. Sheets of nanotubes are called buckypapers and the model and experiments that follow are applicable to them as well. It should be noted that some polymers, like epoxy, shrink upon curing. This causes fiber proximity to decrease which results in increased conductivity since the tunneling shell is now smaller. Recall that network conductivity increases several orders of magnitude for smaller tunneling shells. For these cases, the conductivity is higher for the composite than the pure nanopaper. In this study, the polymer experienced minimal shrinkage upon curing; therefore, the composite is less conductive than the nanopaper.

3.1.1 Carbon Nanopaper

A carbon nanopaper with a high conductivity and good thermal stability is sought after. A carbon nanofiber mat with an areal density of 40 gsm (Applied Sciences, Inc.) was selected for this study. The Pyrograf III nanofibers are highly graphitic and very conductive at lower volume fractions than other fillers [66]. The nanofibers are heat treated to temperatures up to 3000 °C. This graphitizes the chemically vapor deposited carbon present on the surface of the fibers [66]. Additionally, the iron catalyst content is reduced to very low levels. Having these fibers predispersed in sheet form eliminates agglomeration and dispersion defects. The sheet is manufactured using the same techniques and equipment as conventional composites. Tables 3.1 and 3.2 display the material properties of the nanofibers and nanopaper respectively. It can be seen that an individual nanofiber (0.75 S/cm) has a lower conductivity than the nanopaper (6.66 S/cm). For a dense network, mainly parallel pathways exist between the two electrodes. When equating this fiber network to an electrical circuit, the overall resistance decreases for resistors in parallel opposed to series. This results in the nanopaper being more conductive than a single nanofiber.

Table 3.1: Carbon Nanofiber Material Properties

Measure	Value	Unit
Fiber Diameter	60 - 200	nm
Fiber Length	30 - 100	μ m
Fiber Density	1.55 - 1.95	g/cc
Young's Modulus	2.7 - 7.0	GPa
Tensile Strength	400 - 600	GPa
Thermal Conductivity	1950 - 2000	W/mK
Resistivity	1.33	$\Omega \cdot cm$
Electrical Conductivity	0.75	S/cm

Table 3.2: Carbon Nanopaper Material Properties

Measure	Value	Unit
Areal Density	40	gsm
Thickness	0.38	mm
Young's Modulus	2.208	MPa
Peak Load	4.92	N
Peak Stress	11.03	MPa
Failure Strain	0.85	%
Resistivity	0.150	$\Omega \cdot cm$
Electrical Conductivity	6.666	S/cm

The Scanning Electron Microscope (SEM) is used to examine microscopic structures by focusing a beam of electrons that scans over the surface of a specimen. The Zeiss Ultra-55 SEM was used for this study. It employs a Schottky emission source and has an electrostatic final lens compared to a traditional electromagnetic. Schottky electron guns create a strong electrical field to pull electrons away from the atoms. The Ultra-55 has an extra high tension (EHT) acceleration voltage range of 300 V - 20 kV. The InLens Secondary Electrons Detector was used as it is good for high resolution topographic imaging. Figure 3.1 displays how fibers are capable of bridging an insulating gap and how these bridges are broken when strained. Additionally, the random clustering network of these fibers can be observed, as well as the 3D appearance of valleys. The percolating nature of this microstructure provides good piezoresistive behavior since the breaking of junctions will cause a measurable increase in electrical resistance.

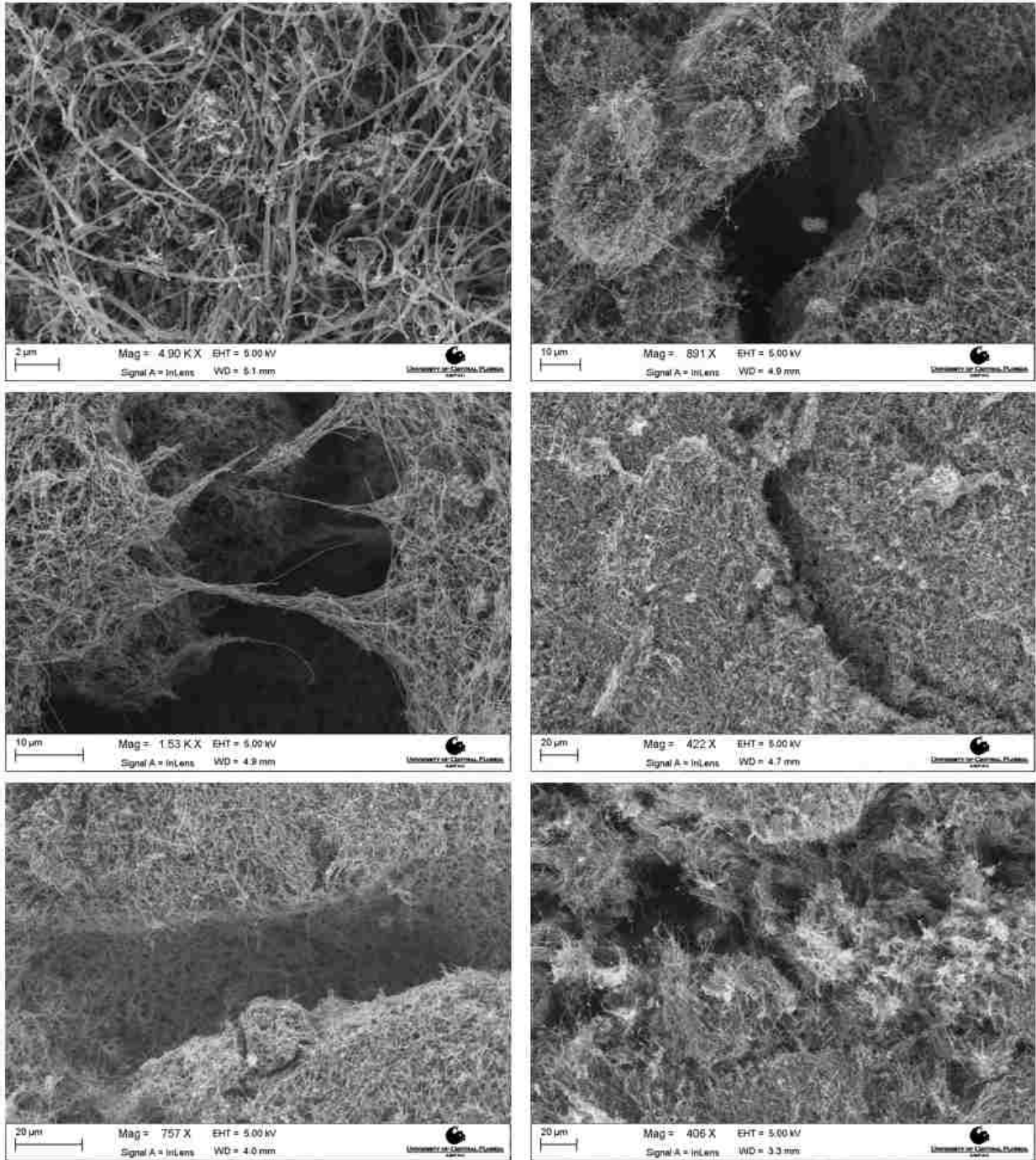


Figure 3.1: Carbon Nanopaper SEM Images

3.1.2 Polymer Matrix

Silicone rubber (Ecoflex-0030, Smooth On Inc.) was selected as the substrate for the composite due to its high strain capabilities, flexibility, biocompatibility, easy processability and low cost [67]. It also bonds well to carbon nanomaterials, has a good temperature range and can conform to complex geometries. Table 3.3 displays the properties associated with this material. These traits make silicone rubber an excellent substrate for human motion detection applications.

Table 3.3: Silicone Rubber Material Properties

Measure	Value	Unit
Specific Volume	939.3	cm^3/kg
Specific Gravity	1.07	g/cc
Young's Modulus	11.0	kPa
Tensile Strength	1.379	MPa
Elongation at Break	587	%
Temperature Range	-53 to 232	°C
Dielectric Strength	13.78	kV/mm
Energy Barrier Height	3.55	eV
Poisson's Ratio	0.47	-
Shore Hardness	OO-30	-

3.2 Composite Fabrication

An acrylic mold was designed for composite manufacturing of a 2.4 mm thick, 13 mm by 130 mm specimen. The mold is made of 1.2 mm thick laser cut acrylic sheets stacked on top of each other and held in place by 10 M4 bolts, washers and wing nuts. A conductive silver paint (SPI Supplies) is used to attach copper leads to the carbon nanopaper to minimize contact resistance in electrical measurements. The copper leads are separated a distance of 26 mm, twice the sample width, thus creating an aspect ratio of 2:1 in the strain sensing region. The carbon nanopaper has a volume fraction of 0.14 in the composite specimen. The silicone rubber is mixed and poured into the

mold and bonded to a rectangular section of carbon nanopaper. Once the first layer has cured, the specimen is flipped in the mold and another acrylic sheet is added to allow for the second layer to be poured. The processing characteristics of the silicone rubber allow for easy manufacturing and creates a good substrate for the fibers. The silicone is easy to mix and pour. It has a mixed viscosity of 3000 cps. Cure time is four hours at room temperature and there is minimal shrinkage, less than 0.0254 mm/mm. As previously mentioned, this minimal shrinkage results in the composite having a lower conductivity than the nanopaper. The finished composite is flexible and has the two copper wires protruding out of the side as seen in Figure 3.2.

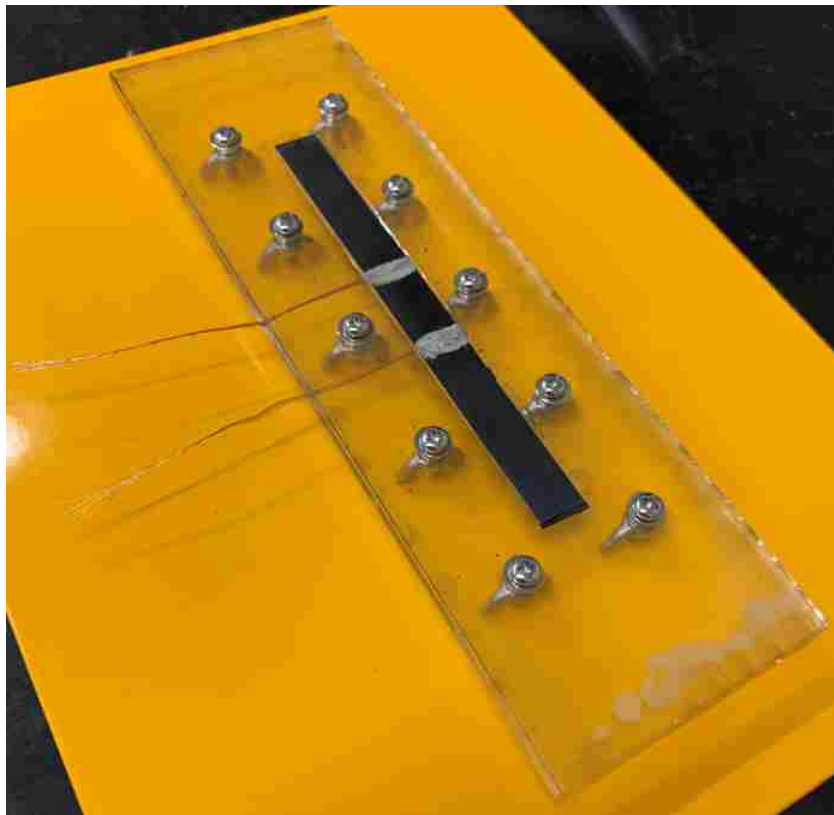


Figure 3.2: Composite Mold

CHAPTER 4: PIEZORESISTIVITY EXPERIMENTAL STUDY

4.1 Materials Characterization

The desired experimental parameters for piezoresistive characterization are initial and deformed state electrical conductivities. The initial state conductivity of the nanopaper and the composite can be measured using a four point probe technique. Electromechanical tests that simultaneously acquire electrical resistance and stress/strain data are used to assess the stretch/release behavior of the composite. The recorded resistances are normalized and used to assess strain sensitivity and linearity.

4.1.1 Four Point Probe Resistivity Measurements

The Four Point Probe Method measures the average resistance of a thin film by applying a current through the outside two points and measuring the voltage across the inside two points. This method is better than traditional two terminal sensing methods since it employs the Kelvin Technique, a way of eliminating wire and contact resistances from a resistance measurement. Since no current flows between the inner two probes, wire and contact resistances do not affect the voltage measured. An accurate resistance is therefore measured between these two probes.

The actual measurement made by the test is V/I . This value is multiplied by a geometrical correction factor, k , to get sheet resistance. The correction factor is dependent on the dimensions of the sample. If the sample is very thin and a square, k has a value of $\pi/\ln(2)$ or 4.53. This k value is used for all tests in this study. Sheet resistance (R_s) is the measure of the resistance between opposite sides of a square and is commonly used to characterize thin conducting films. Sheet resistance has units of Ω/sq . This indicates that the resistance is independent of the size, i.e. length versus width,

of the square since these terms cancel each other out because they are equal. The terminology ohms per square also distinguishes sheet resistance from bulk resistivity. The derivation of the sheet equation for a very thin film follows. Thickness (t) is assumed to be significantly smaller than probe tip spacing, s.

The probe tips emanate current rings on the sample. Area can be expressed as,

$$A = 2\pi tx \quad (4.1)$$

Integrating resistivity (ρ) over area along the probe spacing distance,

$$R_s = \int_{x_1}^{x_2} \rho \frac{dx}{2\pi tx} = \int_s^{2s} \frac{\rho dx}{2\pi tx} = \frac{\rho \ln(2)}{2\pi t} \quad (4.2)$$

From the superposition of current at the outer two probe tips,

$$R_s = \frac{V}{2I} \quad (4.3)$$

Sheet resistance is found by measuring the V/I value,

$$R_s = k \frac{\Delta V}{I} = \frac{\pi}{\ln(2)} \frac{\Delta V}{I} = 4.53236 \frac{\Delta V}{I} \quad (4.4)$$

Resistivity is simply sheet resistance multiplied by the sample thickness,

$$\rho = \frac{\pi t}{\ln(2)} \frac{\Delta V}{I} = R_s t \quad (4.5)$$

The inverse of resistivity is conductivity.

Two 40 mm by 40 mm samples of nanopaper were cut for testing. Each sample was tested twice to ensure accurate results. After a sample underwent its first test, it was rotated 90° for the second test. This allowed the probe points to not overlap on the indentations left by the first test. Nine points per sample were tested in a square pattern on a sample grid of 25 mm as shown in Figure 4.1. The probe tip is made of osmium with a radius of 127 μm and spring loading of 85 g. The spacing between the probes is 1.5875 mm.

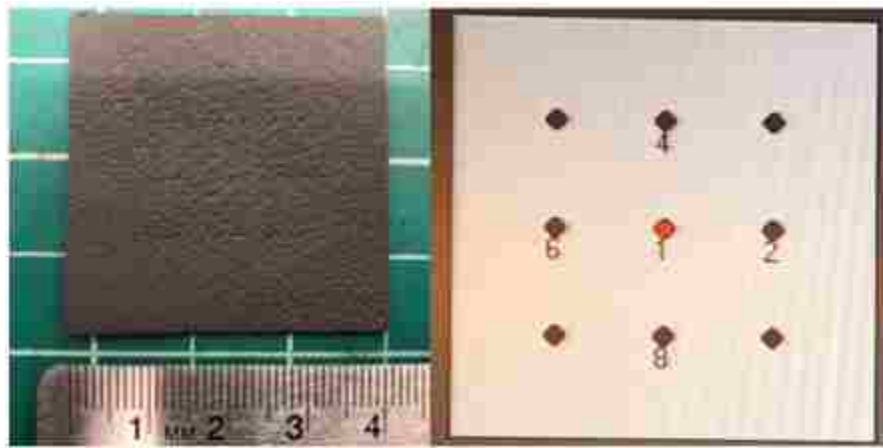


Figure 4.1: Carbon Nanopaper Sample and Square Grid Pattern

A Signatone Quad Pro System used in combination with a Keithley 2400 Sourcemeter was utilized for the tests; displayed in Figure 4.2. For the first measurement, the Quad Pro auto ranges the sourcemeter's current setting to find the best current for testing the sample. All subsequent tests use this current setting. At each site, four different measurements are made according to ASTM Standard F84-99 [68], assuring that errors introduced by the probe head and edge proximity are eliminated, thus increasing the repeatability and accuracy of the measurements. The probe automatically steps to each position and records the x-y position, V/I measurement, sheet resistance and resistivity if thickness is inputted. These results are displayed in Table 4.1.

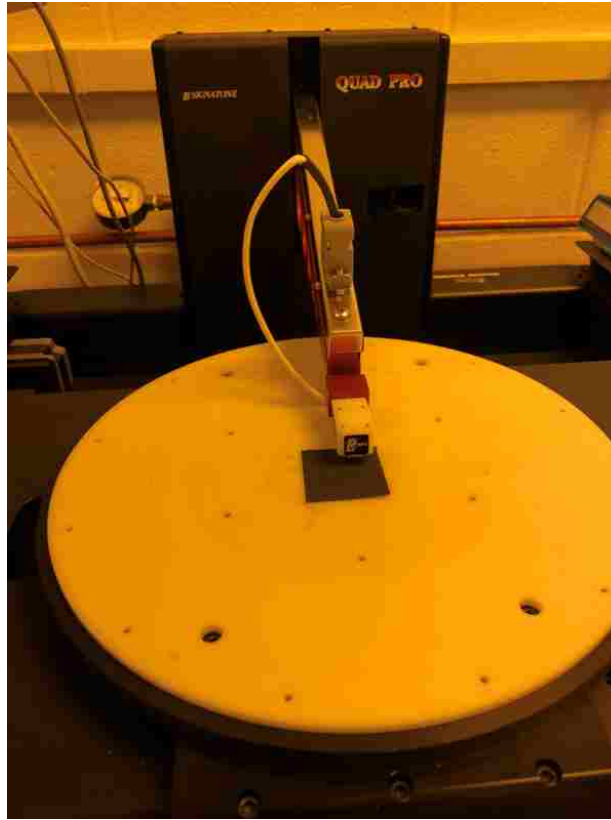


Figure 4.2: Signatone Quad Pro System

Table 4.1: Carbon Nanopaper Four Point Probe Results

	Average	Std. Dev.
V/I	0.885	0.020
Sheet Resistance (Ω/sq)	4.010	0.091
Resistivity ($\Omega \text{ cm}$)	0.150	0.005
Conductivity (S/cm)	6.666	0.005

The resistivity of the composite was measured using the same technique but had four copper wire leads attached to the nanopaper using silver paint and protruding out of the silicone rubber as seen in Figure 4.3. Four measurements were made with a data acquisition system (National Instruments, NI 9219). Results are presented in Table 4.2.



Figure 4.3: Composite Four Wire Measurement

Table 4.2: Carbon Nanocomposite Four Point Probe Results

	Average	Std. Dev.
Resistivity (Ω cm)	0.247	0.0002
Conductivity (S/cm)	4.047	0.002

4.1.2 Electromechanical Tests

Sensing capabilities are studied by several mechanical tests, both monotonic and cyclic, while simultaneously taking resistance measurements as presented in Figure 4.4. Mechanical tests are carried out with an MTS Criterion Model 43 electromechanical universal testing system utilizing a 250 N load cell. Electrical resistance measurements are recorded during tensile tests with a digital multimeter (National Instruments, NI 9219). 10 samples are taken at a sampling rate of 1 Hz within a while loop. The loop wait time is 500 ms. Copper wires are bonded to the nanopaper with a liquid conductive silver paint to create electrodes with minimal contact resistance. A two-wire resistance measurement is made with an excitation current of $500 \mu\text{A}$ and the results recorded in LabVIEW. Time, load, displacement and resistance data are exported for analysis. Cyclic loading

tests are conducted to ensure reliability and repeatability of the composite. The specimen is loaded to various strains and unloaded to zero strain for several cycles.



Figure 4.4: Electromechanical Tests Experimental Setup

4.2 Carbon Nanopaper Piezoresistive Characterization

The experimental piezoresistivity study seeks to assess the relative resistance change for low strains. First, electromechanical tests were carried out on the pure carbon nanopaper. While most material properties are known for the individual fibers, the properties of the paper needed to be assessed. The thin film is very fragile without a substrate; therefore, tests at very low strains were conducted and the resistance changes were likewise very low.

Uniaxial tensile tests are done to acquire the modulus of elasticity and the failure strain of the nanopaper. The failure strain of the pure nanopaper helps to define testing parameters for the composite. The critical strain for the composite specimens is greatly influenced by the pure nanopaper results. A 250 N load cell is used at a crosshead rate of 0.1 mm/min. Data is acquired at a rate of 10 Hz. Fracture tests are first performed to determine the failure strain. A fracture pattern can be observed in Figure 4.5. The nanopaper is extremely fragile and premature failure may be attributed to damage during sample preparation and handling. 130 mm x 13 mm strips of nanopaper are cut from a large sheet. Some damage may have occurred during this process as well as positioning the specimen into the testing grips. An average failure strain of 0.85% was determined from the stress/strain diagram shown in Figure 4.6.



Figure 4.5: Carbon Nanopaper Fracture Pattern

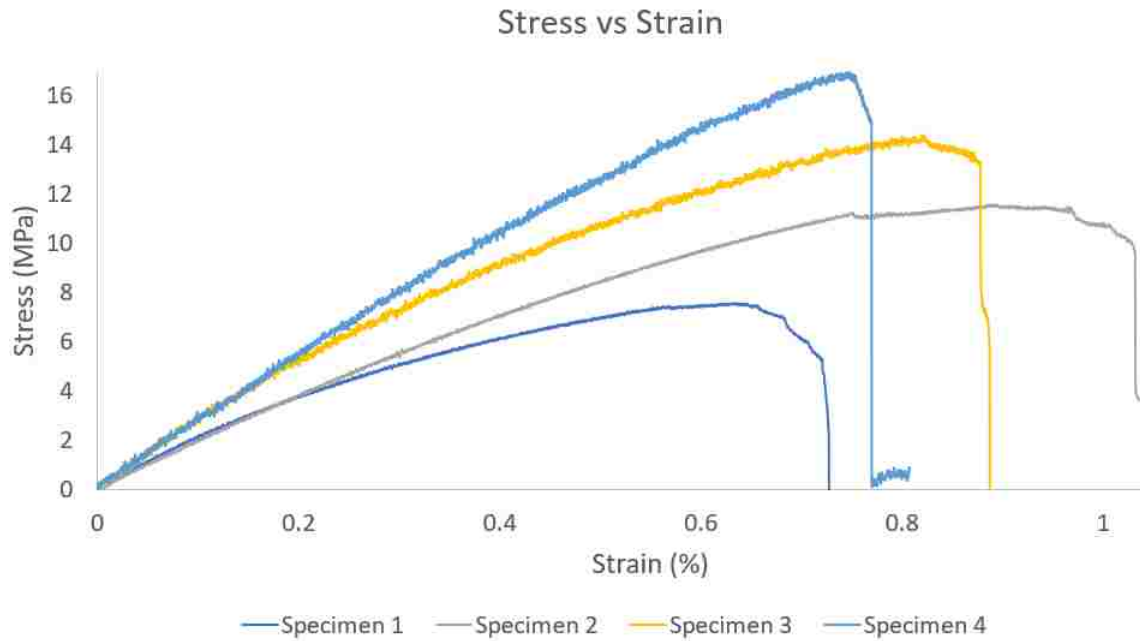


Figure 4.6: Carbon Nanopaper Fracture Test Results

With the failure strain known, resistance measurements can be made during low strain tensile tests. Silver paint is again used to attach copper wires for resistance measurements. Resistance measurements were taken for the paper up to 0.4% strain, about half of the failure strain. The pure paper displays good linearity at very low strains as seen in the resistance change plot in Figure 4.8. Although the resistance changes are very small, the DAQ system is capable of recording accurate data. The rectangular strip of nanopaper with silver paint bond electrodes can be seen in the experimental setup in Figure 4.7.

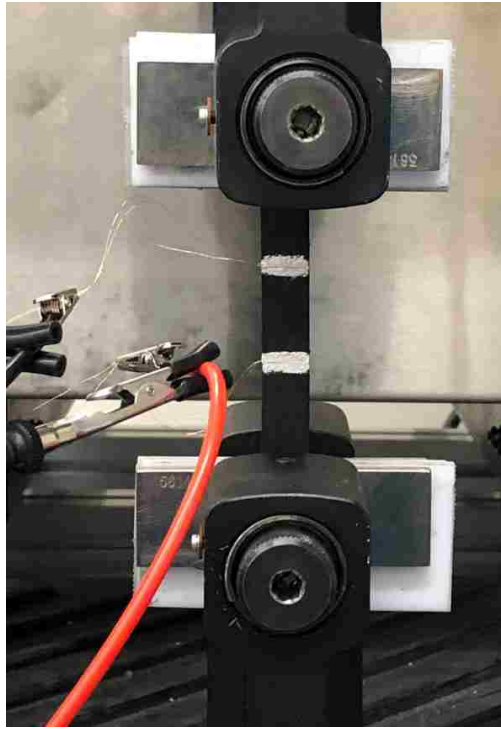


Figure 4.7: Carbon Nanopaper Experimental Setup

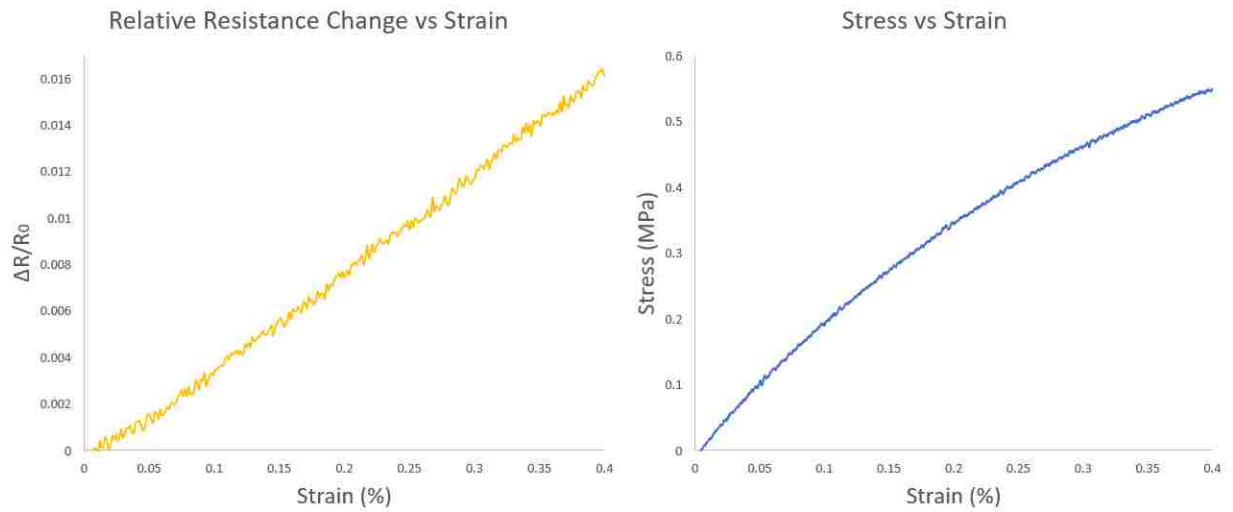


Figure 4.8: Carbon Nanopaper Stretch Results 0.4% Strain

4.3 Composite Piezoresistive Characterization

The composite is tested using the same 250 N load cell at a crosshead rate of 2 mm/min. Spring grips are now used to ensure the sample does not slip as displayed in Figure 4.9. Fracture tests were again conducted first to determine the failure strain at which permanent fiber damage occurs, rendering piezoresistive behavior irrecoverable. This point was found to occur at 3% strain. The following tests were conducted to 2% strain to ensure recoverable piezoresistivity. Resistance and load measurements were taken at a sample rate of 1 Hz. An excitation current of 500 μA was again used for the two wire resistance measurements. Table 4.3 displays measured experimental values.

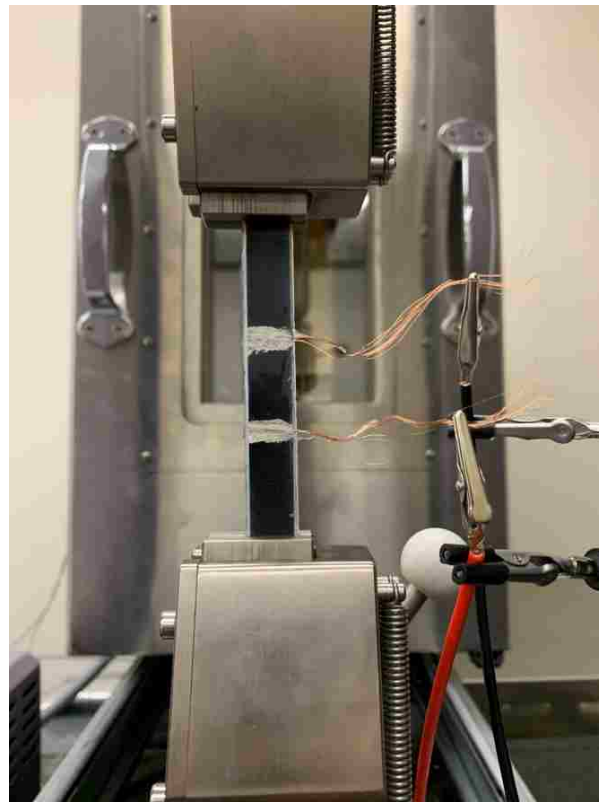


Figure 4.9: Composite Experimental Setup

Table 4.3: Composite Material Properties

Measure	Value	Unit
Density	1.59	<i>g/cc</i>
Thickness	2.14	cm
Young's Modulus	76	kPa
Failure Strain	3	%
Resistivity	0.247	Ω cm
Conductivity	4.047	<i>S/cm</i>

Stretch/release tests are an excellent way to assess the piezoresistivity of the composite. First, results from stretching the composite to 2% strain are presented for better visualization in Figure 4.10. The data has good linearity and matches the strain response well indicating excellent strain sensitivity. The measured resistances show very good proportionality to the strain. The stress/strain plot indicates an elastic behavior.

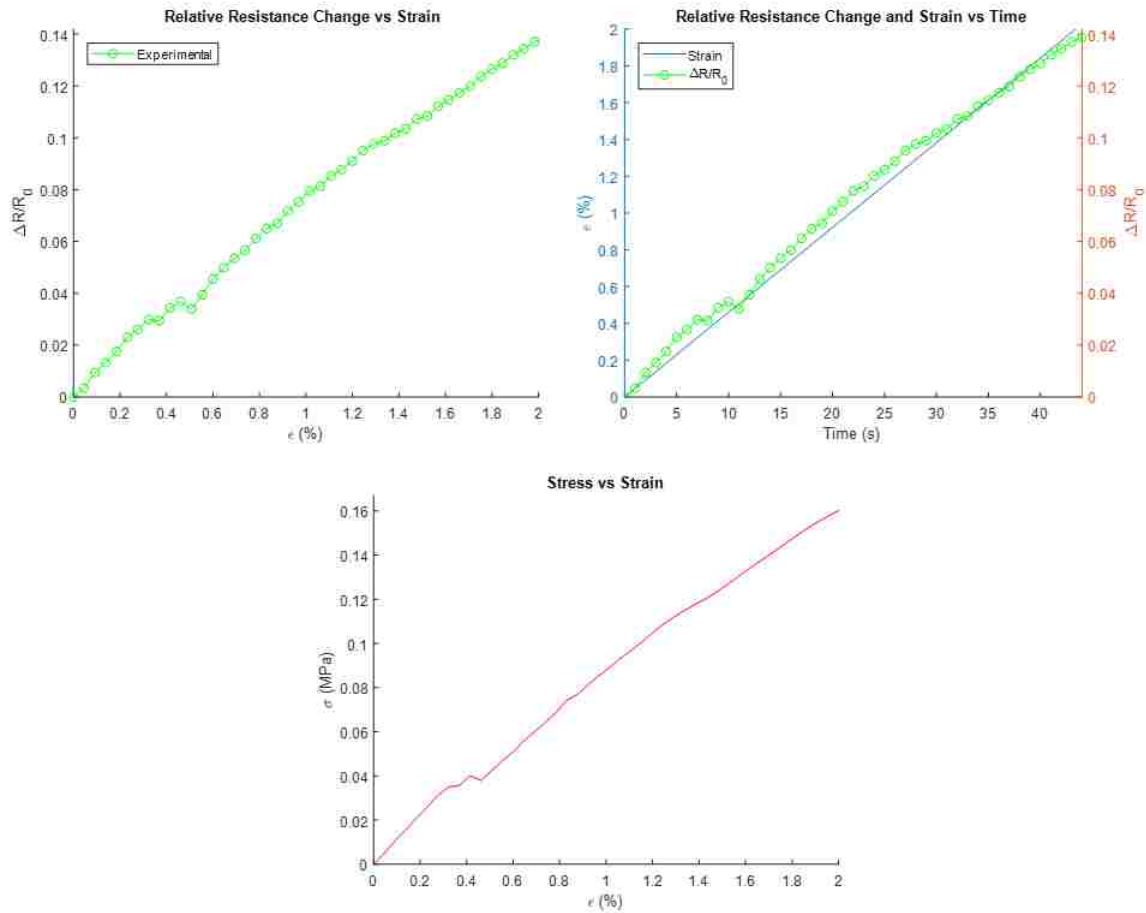


Figure 4.10: Stretch Results 2% Strain

Figure 4.11 display the stretch/release results at 2% strain. While the linearity is not as good in in the upper strain region, the piezoresistivity is recoverable.

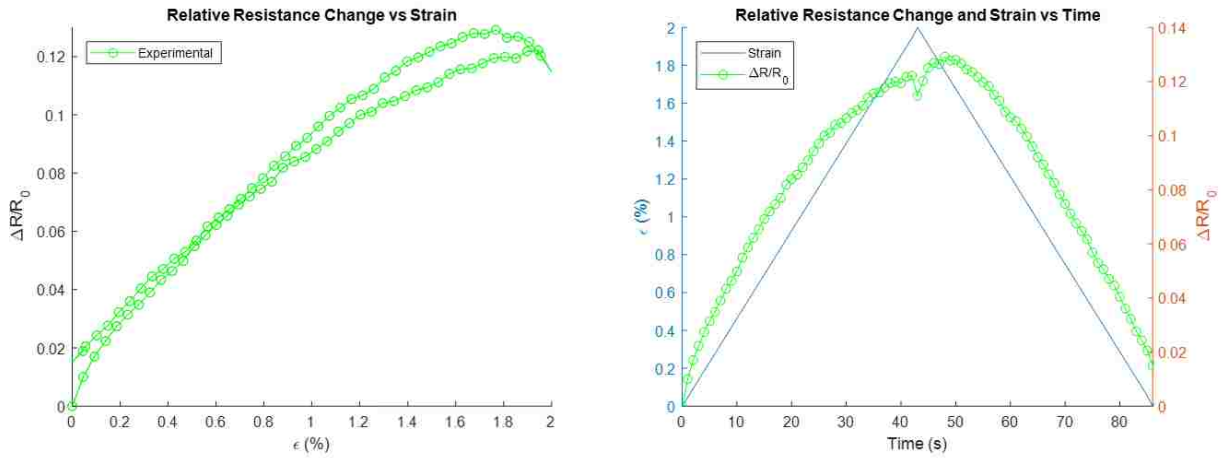


Figure 4.11: Stretch/Release Results 2% Strain

An initial test of three cycles was done. A nonlinear behavior is present for the stretch/release behavior of each cycle in the resistance change versus strain plot. When plotted against time, the resistance measurements are seen to be slightly disproportional to the strain. Hysteresis can be observed in the stress/strain plot of Figure 4.12, highlighting the viscoelastic nature of these materials. The initial stretch is higher than the other cycles due to a preconditioning effect in the fibers. The initial breaking of networks is slightly more intense than the following cycles due to the bonding between fibers and matrix in the fabrication process. This results in a slight stress relaxation in the subsequent cycles. The bonding of the electrodes with the silver paint may have reinforced those regions, causing a slight, albeit undesired decrease in strain sensitivity. Additionally, the slightly negative stress values are due to small discrepancies during the zeroing of the load cell. The 250 N load cell was set as close to zero as possible, but there is some noise present due to the very small loads (<10 N) measured.

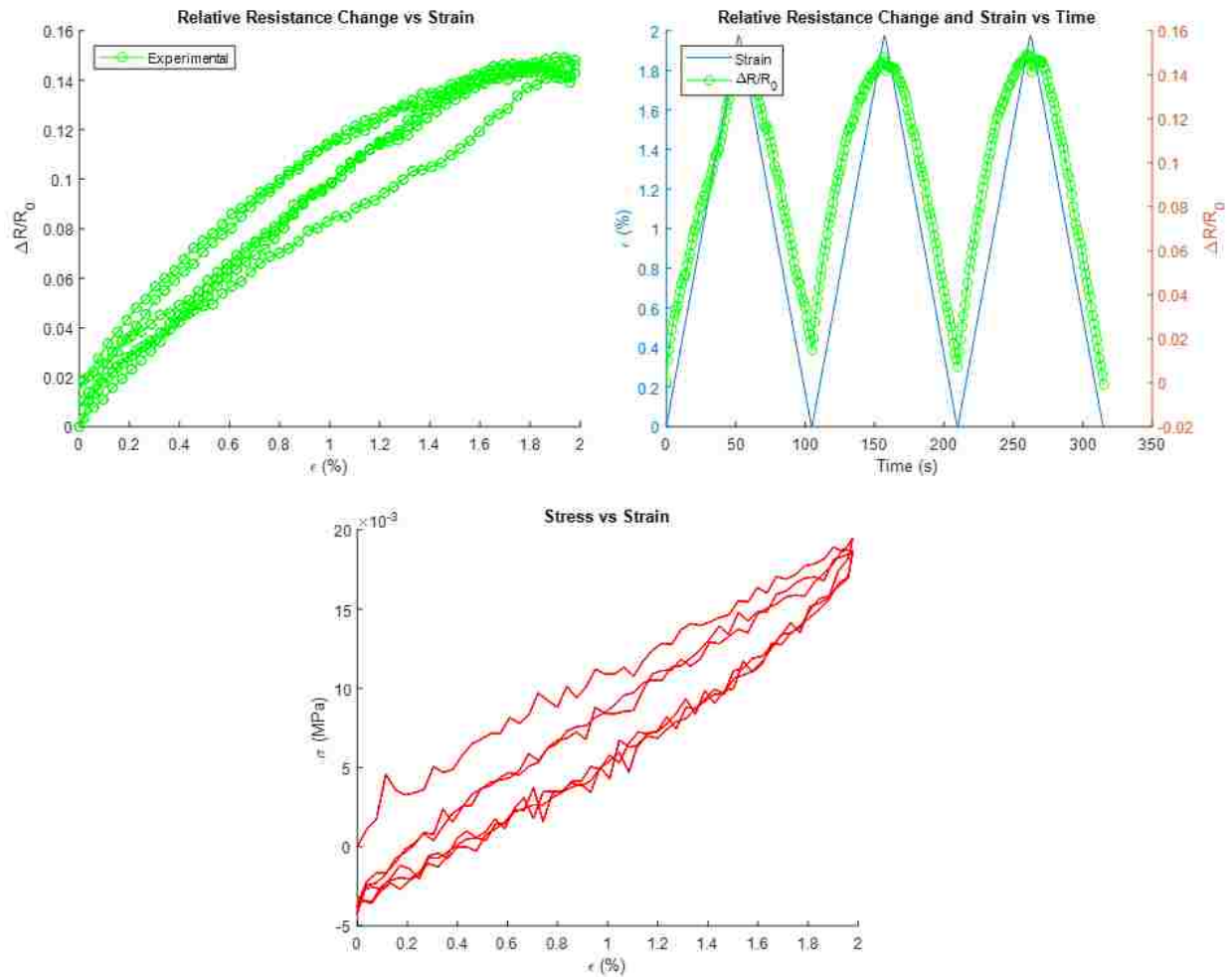


Figure 4.12: 3 Cycle Results 2% Strain

Figure 4.13 displays the first 5 and last 5 cycles of a 15 cycle test for a new specimen. Decent linearity is observed up to 1.4% strain but then, like the previous test, a nonlinear behavior is present. The cycles begin with a consistent behavior and slightly exceed the strain response. The final cycles show how strain sensitivity slightly drops with each cycle. The much wider dispersion in the relative resistance change versus strain plot shows that behavior is less consistent and piezoresistivity not as recoverable as the initial cycles.

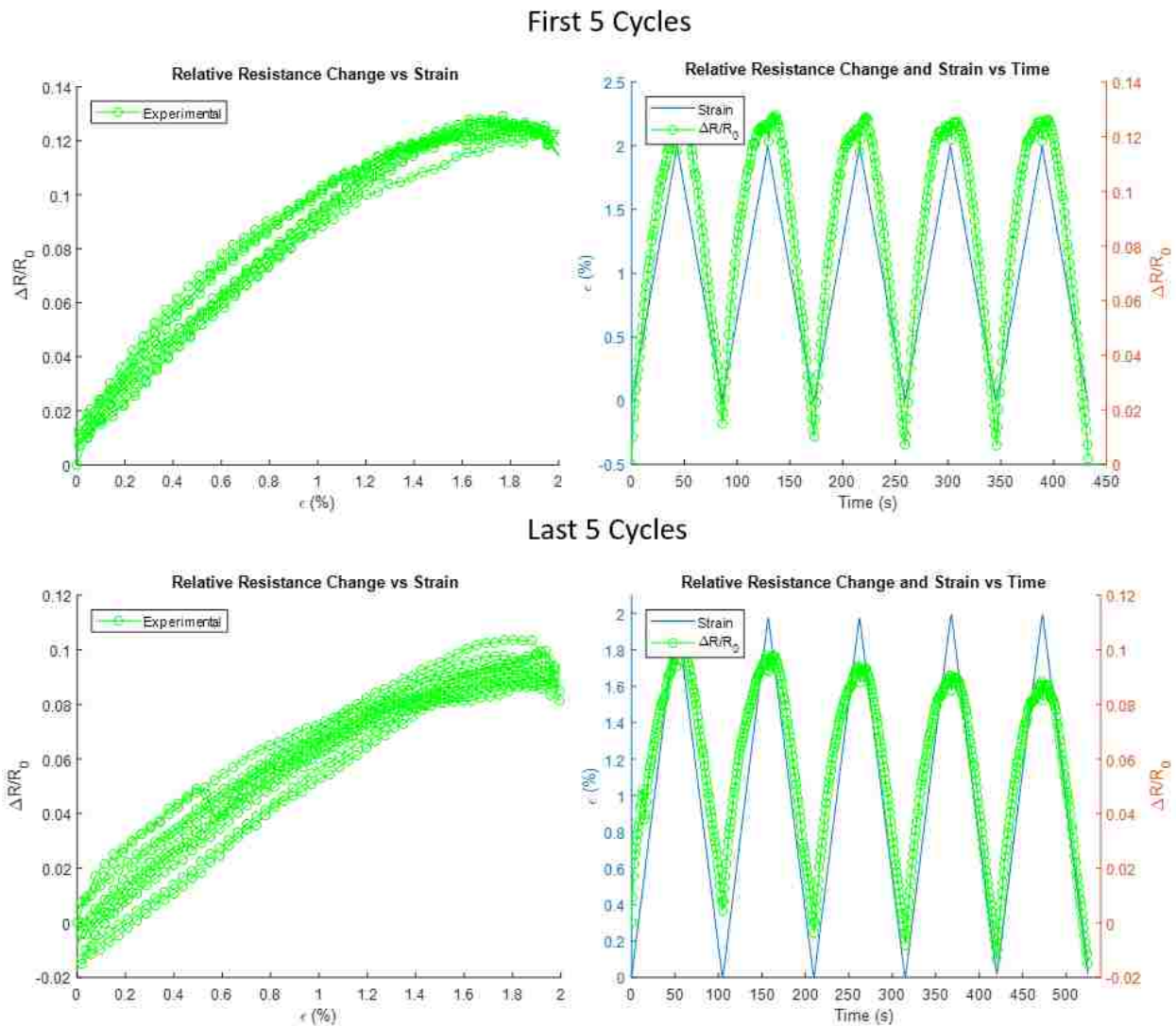


Figure 4.13: 15 Cycle Results 2% Strain

The conducted experiments indicate recoverable piezoresistive behavior at low strains but a slight nonlinearity in the upper strain regions. The fabricated composites were found to have an average gauge factor of 6.625 in the linear strain regions. The first stretch test shows excellent linearity, unlike the following cycle tests. Hysteresis in the stress/strain plots highlight the viscoelastic nature of these materials.

CHAPTER 5: MODEL DEVELOPMENT AND IMPLEMENTATION

5.1 Model Construction

A model predicting the piezoresistive behavior of carbon nanopaper based polymer composites is achieved by determining the electrical conductivity of a generated fiber network for an undeformed and deformed strain state. The relative resistance change is then used to describe strain sensitivity. First, a code written in MATLAB (Mathworks, Inc.) generates randomly oriented fibers and creates a mesh for finite element analysis (FEA). Network geometry, properties, boundary conditions, nodes and elements are all then written as an input file to be solved by electrical circuit simulation in ABAQUS (Dassault Systemes). The resistor network is then solved to determine electrical conductivity of the fiber network.

Functions were created to carry out particular tasks and are simply called in the main code. The implementation of these functions in the main code is now discussed in detail. The first section of the main code consists of defining parameters and inputting known variables. These input parameters are displayed in Table 5.1. Fiber and matrix properties as well as physical constants are also defined. The number of fibers used is estimated based on the percolation threshold for the selected unit cell.

It should be noted that this model is for strain sensing at a constant temperature and is therefore linear in nature. Mechanical, electrical and thermal properties are related, and any heating actuation or operation in varying temperature ranges results in a nonlinear system.

Table 5.1: Material Properties Input Parameters

Nanofibers	Matrix	Composite
Nanofiber Diameter	Poisson's Ratio	Tunneling Distance
Nanofiber Length	Energy Barrier Height	Tunneling Conductivity
Number of Fibers		

5.1.1 Microstructure Generation

A unit cell is first defined by a set length (a) and height (b). Next, the electrode boundaries are defined and generated. The source electrode is on the left and has height b. The drain electrode is to the right of the source by length a, also with height b. The length, diameter and number of fibers are inputted into the function. Fibers are generated in 2D space by defining their center coordinates (x_c, y_c) and orientation (θ). The MATLAB rand function is used to generate uniformly distributed random numbers between 0 and 1. Fiber center coordinates and orientation angles are randomly generated using this function. The number of fibers, N, is inputted based on the fiber volume fraction and the requirement of being at or above the percolation threshold. For this model, fibers are flat rectangles of a defined length and width.

$$x_c = a \times rand(1, N) \quad (5.1)$$

$$y_c = b \times rand(1, N) \quad (5.2)$$

$$\theta = \sin^{-1}(1 - 2 \times rand(1, N)) + \frac{\pi}{2} \quad (5.3)$$

One fiber is created at a time inside a for loop for $k = 1:N$ fibers using complex analysis. A nested for loop is used to solve the positive and negative parts of the following complex equation. Fibers are plotted inside the unit cell with length L as seen in Figure 5.1.

$$z = x_c(k) + iy_c(k) \pm \frac{L}{2} e^{-i\theta(k)} \quad (5.4)$$

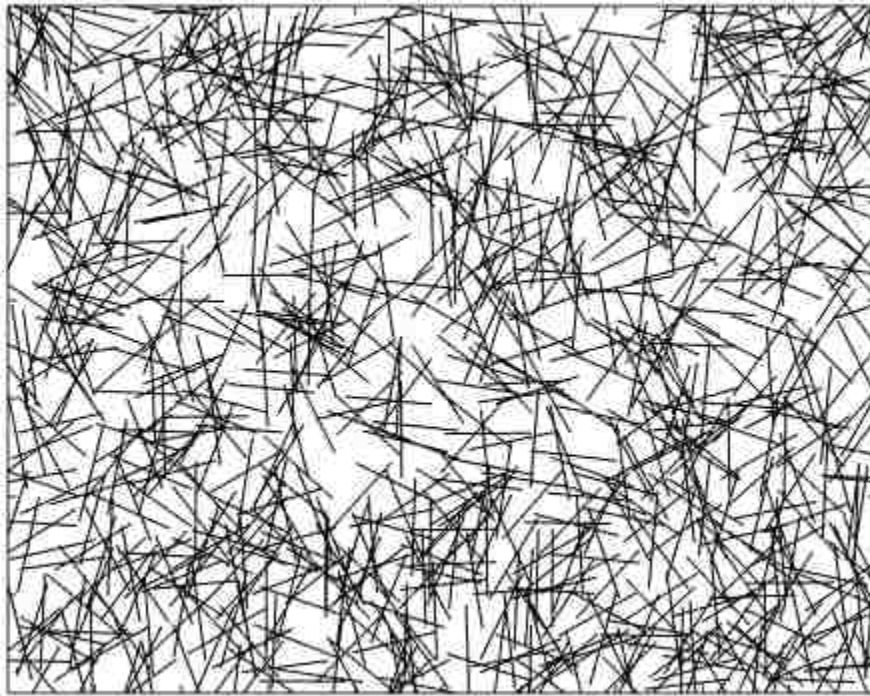


Figure 5.1: 2D Fiber Generation

Fibers are sorted into columns where the real part of the z equation provides the x coordinates and the imaginary part provides the y coordinates. The coordinates for the starting and ending points of all fibers are also recorded.

5.1.2 Fiber Intersection

In 2D, the intersection of two fibers can be found using a method of determinants. The starting coordinates (x_1, y_1) and ending coordinates (x_2, y_2) were defined in the fiber generation function. Now, these points are checked with all other fiber coordinates (x_3, y_3) and (x_4, y_4) .

$$x_{intersect} = \frac{\begin{vmatrix} x_1 & y_1 & 1 \\ x_2 & y_2 & 1 \end{vmatrix} \begin{vmatrix} x_3 & 1 \\ x_4 & 1 \end{vmatrix}}{\begin{vmatrix} x_1 & 1 \\ x_2 & 1 \end{vmatrix} \begin{vmatrix} y_3 & 1 \\ y_4 & 1 \end{vmatrix}} \quad (5.5)$$

$$y_{intersect} = \frac{\begin{vmatrix} x_1 & y_1 & 1 \\ x_2 & y_2 & 1 \end{vmatrix} \begin{vmatrix} x_3 & 1 \\ x_4 & 1 \end{vmatrix}}{\begin{vmatrix} x_1 & 1 \\ x_2 & 1 \end{vmatrix} \begin{vmatrix} y_3 & 1 \\ y_4 & 1 \end{vmatrix}} \quad (5.6)$$

Since two non-touching and non-parallel lines intersect at some point beyond their lengths, a conditional statement is applied to only record the intersection coordinates along a fiber's length. Additionally, the intersections of fibers with the left and right boundaries are recorded, as the boundaries represent the source and drain electrodes. As will later be seen in the simulations, some fibers penetrate the unit cell. Since there are a high number of fibers in the unit cell in order to meet or exceed the percolation threshold, periodic boundary conditions are not applied. The representative volume element is made to be sufficiently large enough to represent the composite.

Figure 5.2 illustrates the location determination of the fiber intersections.

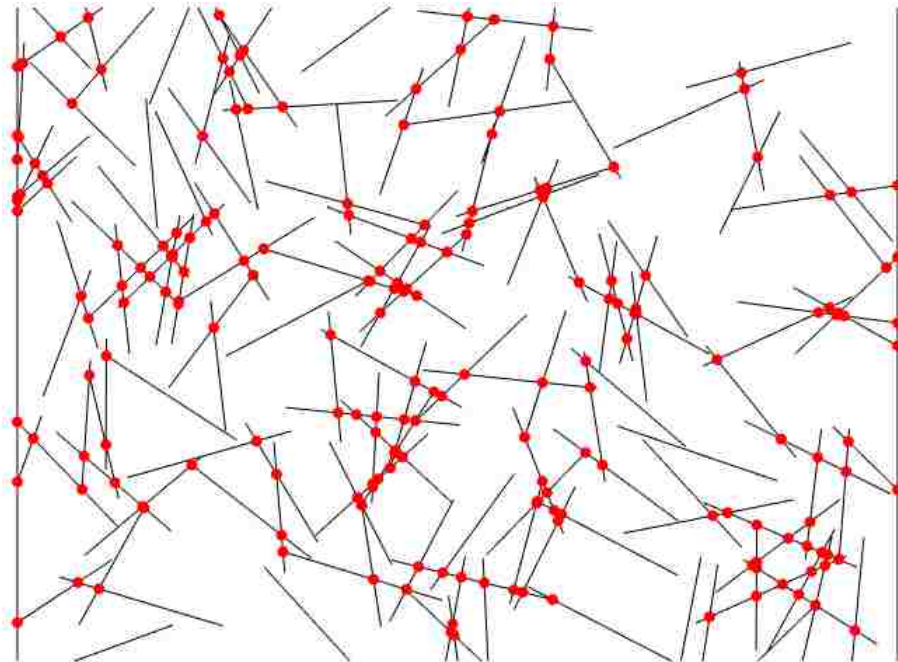


Figure 5.2: Fiber Intersection

5.1.3 Mesh Generation

A mesh is created by the MATLAB code before being exported for FEA. First, nodes are created at all fiber end points. These nodes were generated in conjunction with the fibers. In order for finite element analysis to take place, two intersecting fibers must share a node at the intersection point. However, in the intersection function, a node is placed at an intersection point for all fibers. This results in stacked nodes, which would cause the FEA to fail. A new function is therefore implemented to merge stacked nodes. This is achieved by constructing a symmetric numbering matrix which identifies which two nodes share an intersection point. One of these nodes is then removed and the mesh is fully generated. This allows the flow of current through the network in

the electrical simulation. Generated nodes at all fiber endpoints and intersections can be seen in the mesh in Figure 5.3.

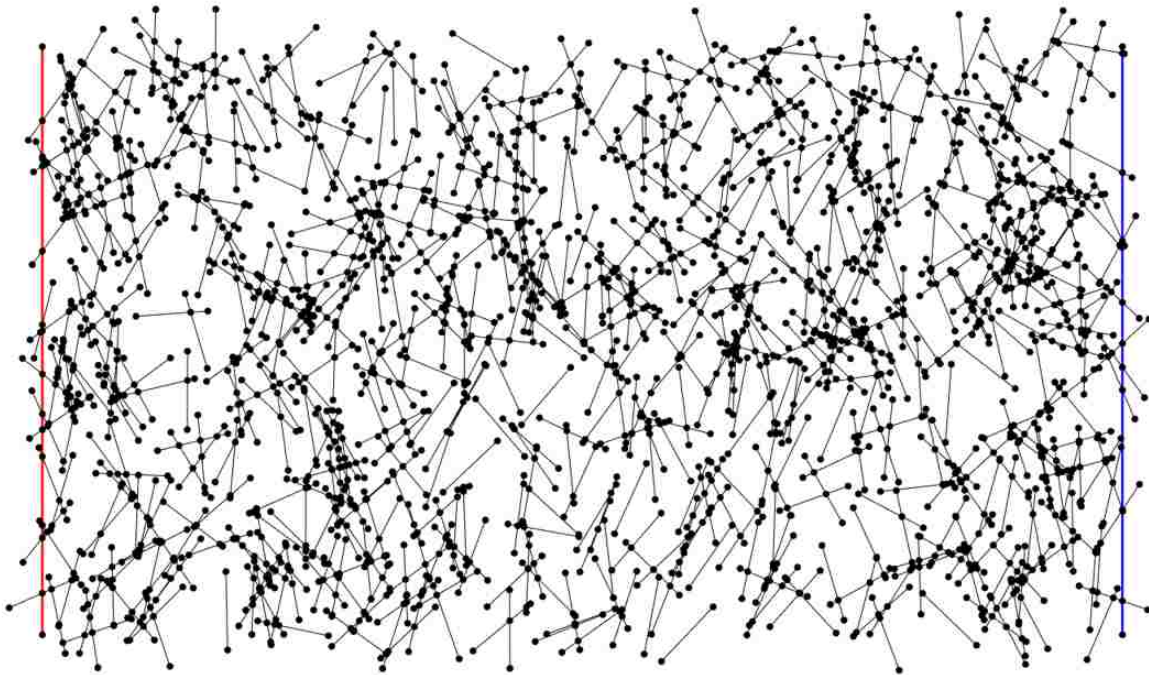


Figure 5.3: Fiber Network Mesh

The manner in which all the aforementioned data created in MATLAB is exported to ABAQUS is through an input file. Essentially, all the FEA procedures required through the graphical user interface can be eliminated since the geometry, nodes, elements, boundary conditions, element type and output variables are all stated in the input file. The MATLAB code generates this file directly which can be submitted as a job to ABAQUS. The results can then be viewed after a quick computation time, without the need of any user interaction. This automation is particularly beneficial for Monte Carlo simulations, where a high number of runs are required. One dimensional truss elements are used for the fibers. In particular, 2-node link, coupled thermal-electrical elements are used. Since 1D truss elements are being used, it has been deemed acceptable to only place nodes

at fiber endpoints and intersections. Refining the mesh has an insignificant effect on the results for circuit simulations of this type. Appendix A contains all the MATLAB code used in this study and Appendix B contains the ABAQUS input file for a simple case of 5 fibers.

5.1.4 Equivalent Resistor Network Formation

Before the resistor network can be analyzed, the tunneling conductivity of the generated fiber network must be determined. The tunneling resistance can be determined for a single junction by knowing the cross-sectional area of the tunnel, which is approximated as the square of fiber diameter, energy barrier height λ , and the tunneling thickness, t . Energy barrier heights and tunneling thicknesses have defined ranges as previously discussed and their values are available in literature. Once the tunneling resistance for a junction is known, it is converted to resistivity by multiplying it by fiber cross-sectional area and dividing by the tunneling distance. Taking the inverse gives the conductivity at a junction.

$$\sigma_{tun} = 1 / \left[\frac{h^2}{q_e^2 \sqrt{2m_e \lambda}} \exp\left(\frac{4\pi}{h} \sqrt{2m_e \lambda t}\right) \right] \quad (5.7)$$

Since tunneling is the dominant form of electron transport, it is assumed at all junctions in the network. In FEA, a material property cannot be assigned to a node, so a new command is created in MATLAB to determine the number of junctions for the generated network. This is done by simply using logic to find the number of intersections. A logic matrix of zeros and ones is assembled. The nonzero elements of the intersection matrix are counted and yield the number of junctions in the network. This number is multiplied by the junction conductivity to get overall tunneling conductivity for the whole network.

With the parameters defined in the input file, electrical simulations can now commence. Ni et al. [69] obtained the equivalent resistance from the nodal voltage distribution by solving the system of linear equations with a Gaussian Elimination Method. This same theory is used, except in this study, the equivalent resistance is solved by finite element analysis. For dense networks, mainly parallel pathways exist between the electrodes; therefore, resistances are solved for parallel circuits. Figure 5.4 illustrates this concept.

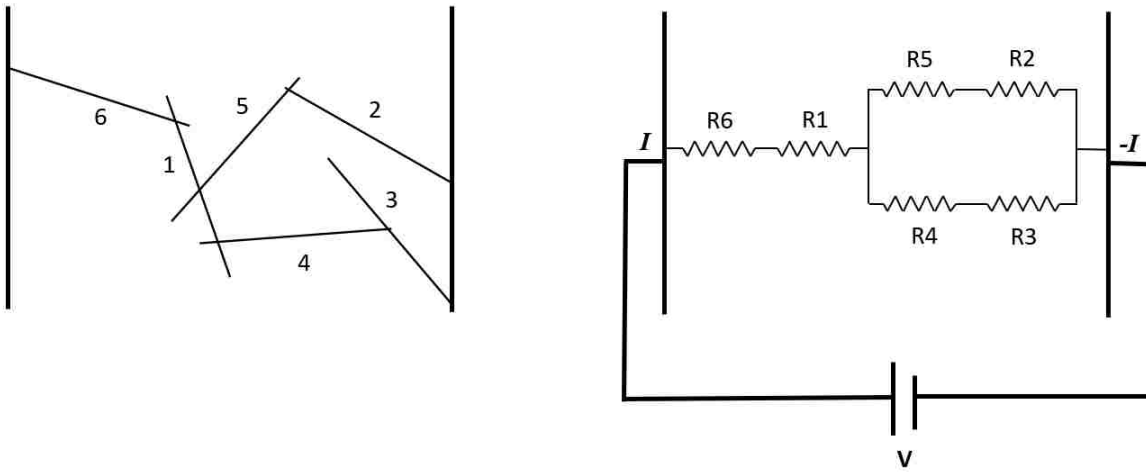


Figure 5.4: Circuit Representation of Fiber Network

The conductance (g) between two intersecting points can be calculated by,

$$g_{ij} = \sigma_{CNF} \frac{A_{CNF}}{l_{ij}} \quad (5.8)$$

σ_{CNF} is the fiber conductivity, l is the distance between two intersecting points and A is fiber cross-sectional area.

The matrix representation for a resistor network and Kirchhoff's current law are used to solve for the total current under an applied voltage. The sum of the currents for the fibers touching the

source electrode is equal to I and the sum of the currents for the fibers touching the drain electrode is equal to -I. The conductance matrix (G) variant of Ohm's Law can be solved for a known electric potential to determine the current in the network.

$$\begin{vmatrix} G_{11} & \dots & G_{1N} \\ \vdots & \ddots & \vdots \\ G_{N1} & \dots & G_{NN} \end{vmatrix} \begin{vmatrix} V \\ \vdots \\ 0 \end{vmatrix} = \begin{vmatrix} I \\ \vdots \\ I_N \end{vmatrix} \quad (5.9)$$

The top row is for the source electrode and the bottom row is for the drain electrode.

5.1.5 Electrical Conductivity Determination

Current density (J) is current per cross-sectional area. Electrical conductivity can be determined by summing the currents touching the source electrode. The MATLAB code defined a set of which fibers touch the source electrode. This allows for easy calculation in ABAQUS as the source fibers or drain fibers can be selected and the currents summed. Kirchhoff's law applies to the summation at any junction. It is the same for the source or drain electrodes. Electrical conductivity can be solved by using Ohm's Law.

$$\sigma = J/E \quad (5.10)$$

E is the electric field which in this case is simply the applied voltage. Figure 5.5 highlights the fibers touching the source electrode and sums the currents occurring at the corresponding nodes. This summation provides the current density for the whole network. Contour plots of the electrical current density and voltage are then created.

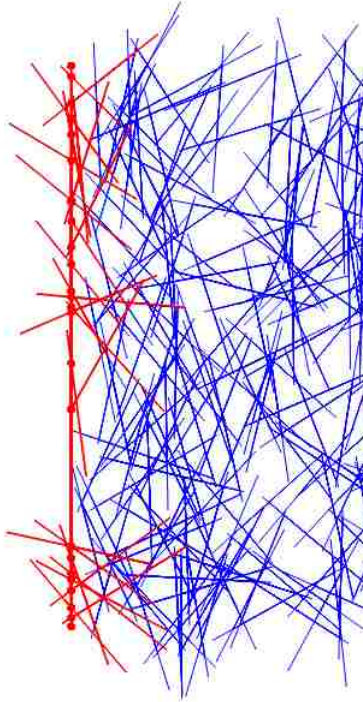


Figure 5.5: Current Summation at Source Electrode

5.1.6 Deformation of the Microstructure

When a strain is applied to the composite, the distance between fibers may increase and fiber orientation may change, causing the tunneling vector length and direction to change. Additionally, the path required for electrons to flow is longer and junctions may break. Both result in an increase in resistance. The relative resistance change as a function of strain can then be calculated analytically by knowing the initial and final electrical conductivities of the composite. The conductivity for a certain strain is calculated the same way as the undeformed composite once fiber positions and orientations are updated. Several assumptions for the deformation are made. Strain is assumed to be low and uniaxial. Carbon nanomaterials have a significantly higher Young's modulus than the polymer matrix; therefore, they are considered as rigid bodies. Fiber rotational movement is

dependent on the matrix. The same tunneling shell for the reference state is assumed at all contact junctions for the deformed state.

A deformation gradient is applied to the unit cell. The stretching and bending of fibers are neglected. The following equations take the original (x, y) coordinates to update fiber positions and orientations. The deformation is symmetric about the x -axis through the center of the unit cell. Unit cell height, b , decreases accordingly to the strain about this symmetry axis. For the strained composite, the simulation is run again after updating the new fiber positions and orientations.

$$x' = x(1 + \epsilon) \quad (5.11)$$

$$y' = y - \nu\epsilon(y - b/2) \quad (5.12)$$

The source electrode side remains fixed while the drain electrode side is pulled. Figure 5.6 illustrates the deformed network (green) in comparison to the original network (black). It can be seen that fibers closer to the drain electrode change position more so than the other end. It is also important to recall that the defined strains must be below the critical strain as permanent deformation occurs beyond this value, rendering irrecoverable piezoresistive behavior.

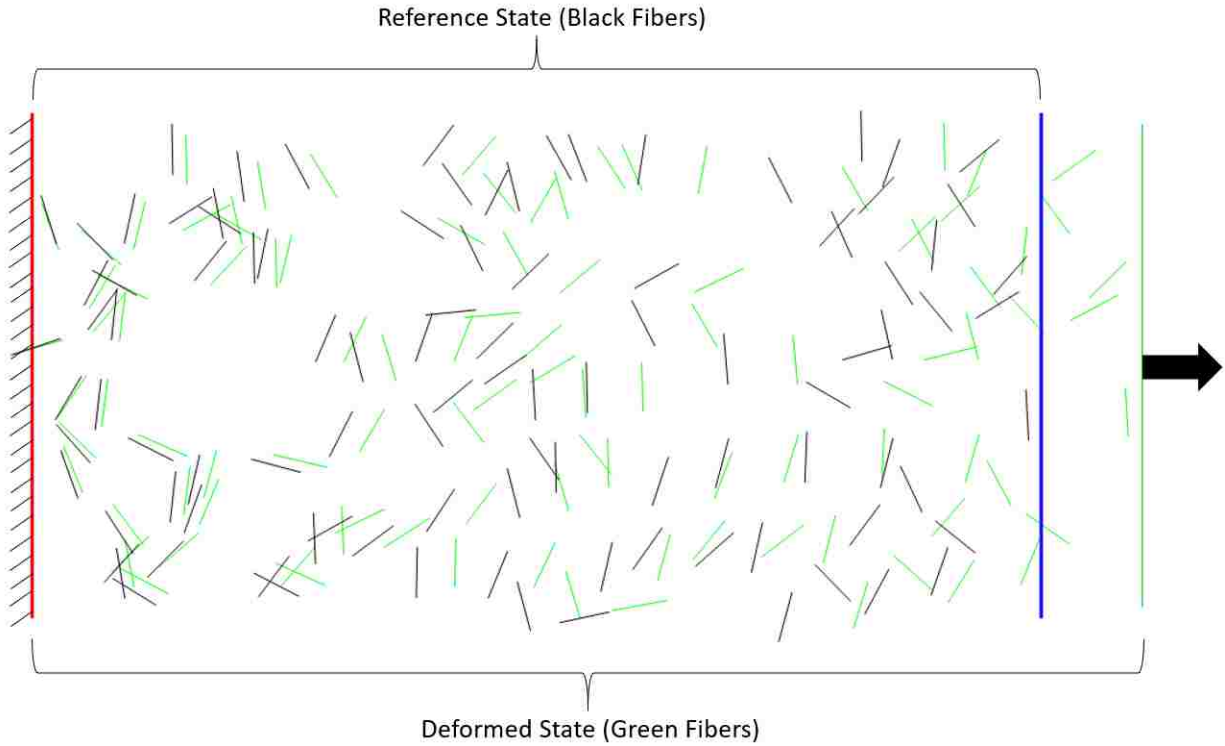


Figure 5.6: Deformed Fiber Network

A simple piezoresistive model can be developed once the conductivities for the undeformed and strained states are known. Recalling that the relative resistance change as a function of strain can be expressed as,

$$\frac{\Delta R}{R} = \frac{\rho L A_0}{\rho_0 L_0 A} - 1 \quad (5.13)$$

The change in length and area due to strain can be expressed as,

$$L = (1 + \epsilon)L_0 \quad (5.14)$$

$$A = (1 - \nu\epsilon)^2 A_0 \quad (5.15)$$

Substituting these equations and changing resistivity to conductivity,

$$\frac{\Delta R}{R} = \frac{\sigma_0}{\sigma_f} \cdot \frac{(1 + \epsilon)}{(1 - \nu\epsilon)^2} - 1 \quad (5.16)$$

This equation is a simple way to predict the piezoresistive behavior of the composite after the numerical conductivity simulations.

5.2 Sensitivity Study of Input Parameters

The same carbon nanofibers in the experimental study were modeled in the simulation. The nanopaper has an areal density of 40 gsm. The unit cell dimensions and number of fibers were selected to best represent the percolation threshold. Fiber length and diameter are estimated based on the variations provided by the manufacturer and the fact that the fibers in this model are defined as straight lines. The same silicone rubber matrix is used as the substrate with a Poisson's ratio of 0.47.

Key input parameters were varied to assess their impact on model results and determine a specific value that best represents the proposed materials. Many simulations were run in a back and forth manner to observe how network conductivity changes with a single parameter variation. The parameters that were assessed were fiber length, diameter and concentration, tunneling shell, energy barrier height and applied voltage. One parameter was varied while all others were fixed at their final determined value. An assessment of these variations follows presenting the conclusions in a logical order. All values reported represent the averages of many simulations.

5.2.1 *Fiber Dimensions and Concentration*

All fibers have the same length and diameter and are straight lines. The nanopaper manufacturer provided average values for fiber length and diameter. These values were verified using the SEM micrographs. A fiber diameter of 200 nm and fiber length of 100 μm were deemed acceptable to represent the network. Since this is a 2D model, areal density is difficult to match to the actual nanopaper. The nanopaper thickness is equivalent to 1900 stacked fiber diameters. Therefore, the number of fibers to achieve percolation is sought after. Once this value is known, variations in fiber length and diameter can be assessed.

A rectangular representative volume element with a 2:1 aspect ratio was selected for both the simulations and experiments. The simulation unit cell is 20 fiber lengths long. 2000 fibers were initially estimated to represent the density of the network. The number of fibers was adjusted after several cases to determine the percolation threshold. Figure 5.7 contains several voltage plots which illustrate the percolating nature of fiber networks. All cases were supplied a 10 V electric potential. Fibers with lengths of 100 μm , diameters of 200 nm, tunneling shell of 1 nm and energy barrier height of 3.55 eV were the fixed parameters.

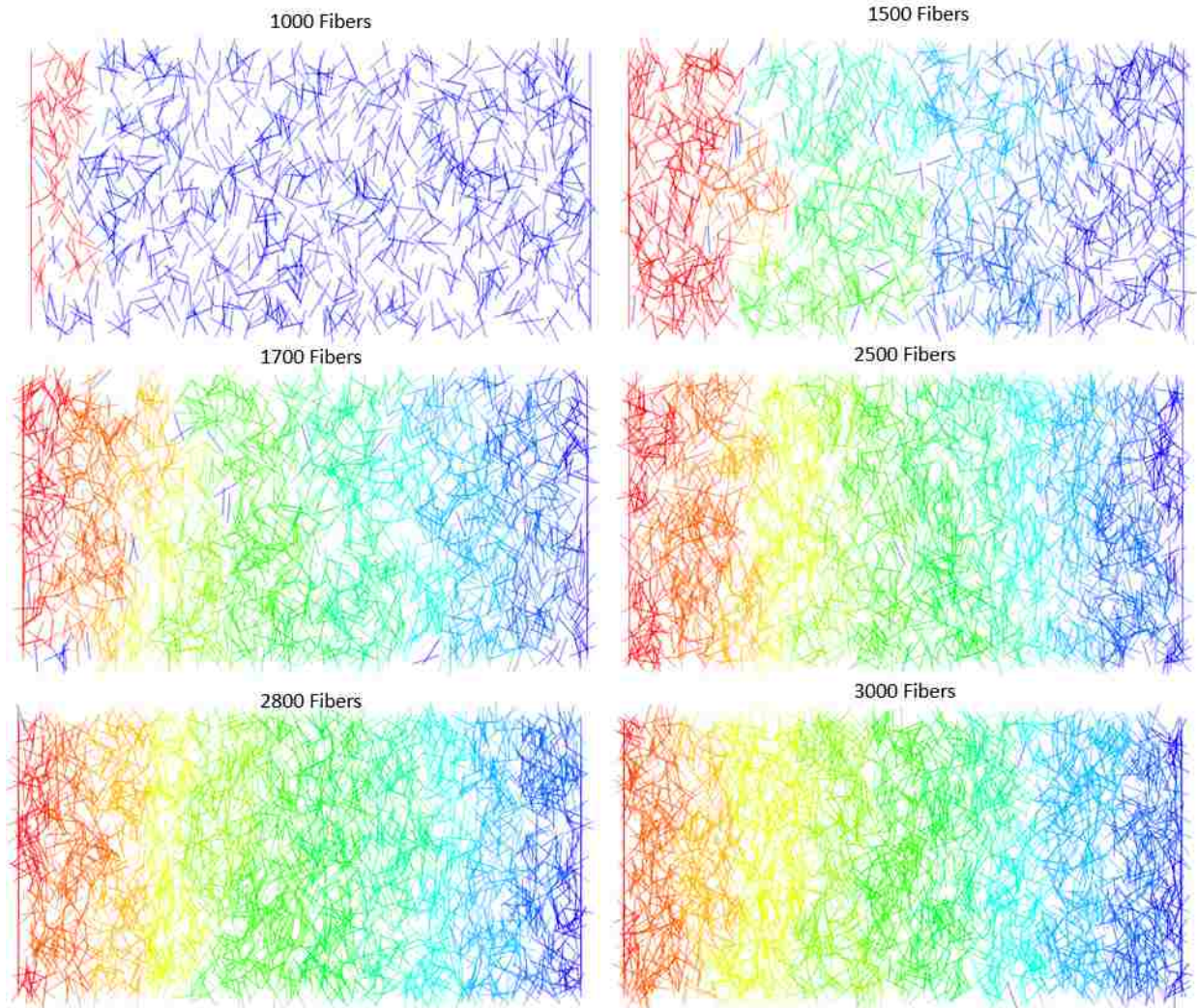


Figure 5.7: Percolation Voltage Contours for Increasing Number of Fibers

The voltage contours display the insulator to conductor phase transition. The determined network conductivities can be plotted for increasing number of fibers to reveal the percolation trend. Figure 5.8 indicates that the percolation threshold occurs at 2800 fibers. 3000 fibers were used for the following simulations as it is just above the percolation threshold. Again, fiber volume fractions just above this threshold exhibit the most sensitive piezoresistive behavior.

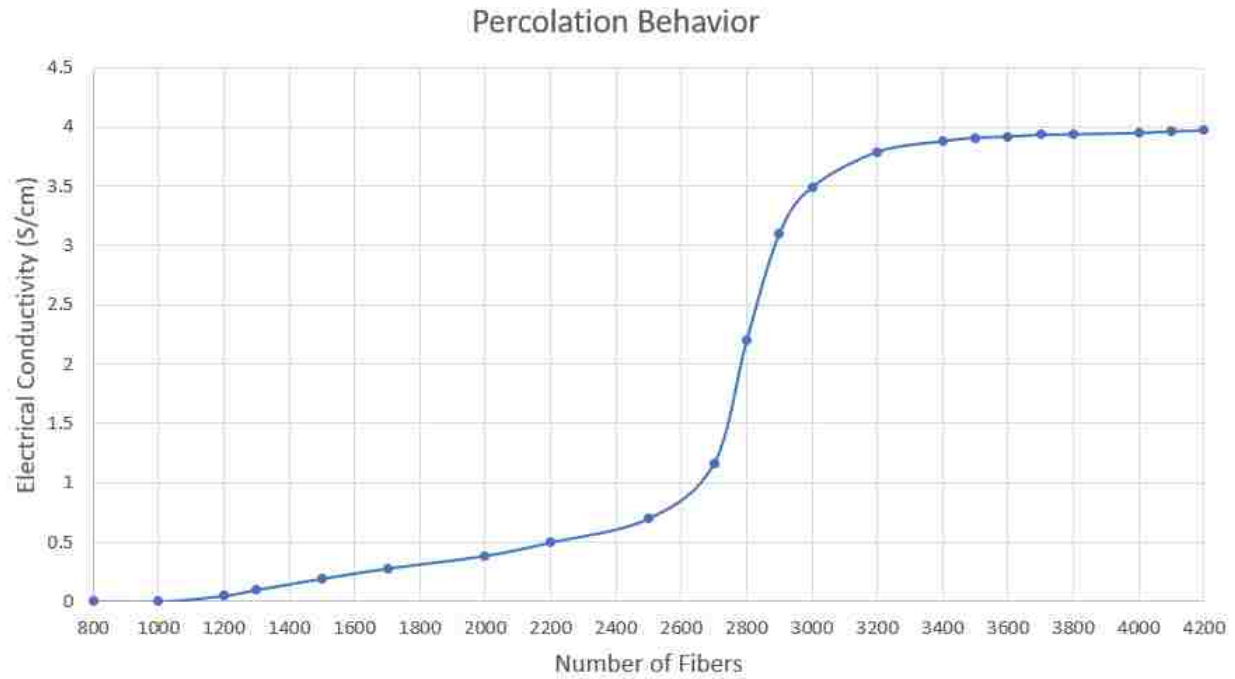


Figure 5.8: Percolation Behavior of Fiber Network

Fiber diameters were varied from 100 to 300 nm. 3000 fibers with lengths of 100 μm , tunneling shell of 1 nm and energy barrier height of 3.55 eV were the fixed parameters. Since the fibers have a very high aspect ratio, 500, changes in diameter have an insignificant change on network conductivity as seen in Figure 5.9. A near constant value of 3.42 S/cm was determined for all variations.

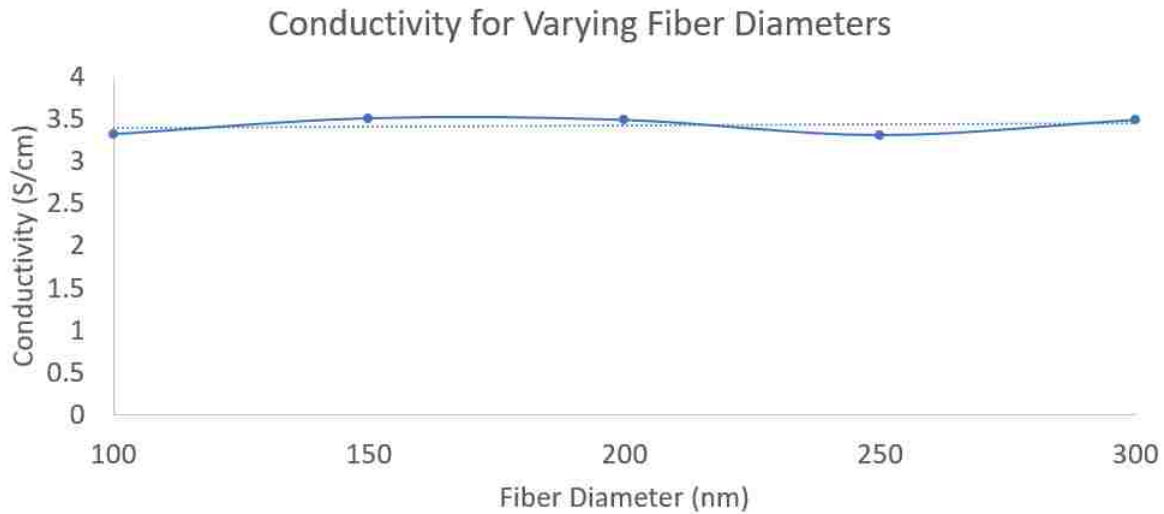


Figure 5.9: Conductivity Changes for Varying Fiber Diameters

The number of fibers selected was dependent on the fiber length. Now, conductivity is assessed when the number is fixed at 3000 fibers and the length varies from 50 to 200 μm . Fiber diameter of 200 nm, tunneling shell of 1 nm and energy barrier height of 3.55 eV are the fixed parameters. Figure 5.10 illustrates how percolation is significantly easier to achieve with increasing fiber lengths. Fiber lengths beyond 150 μm do not display a well defined voltage contour.

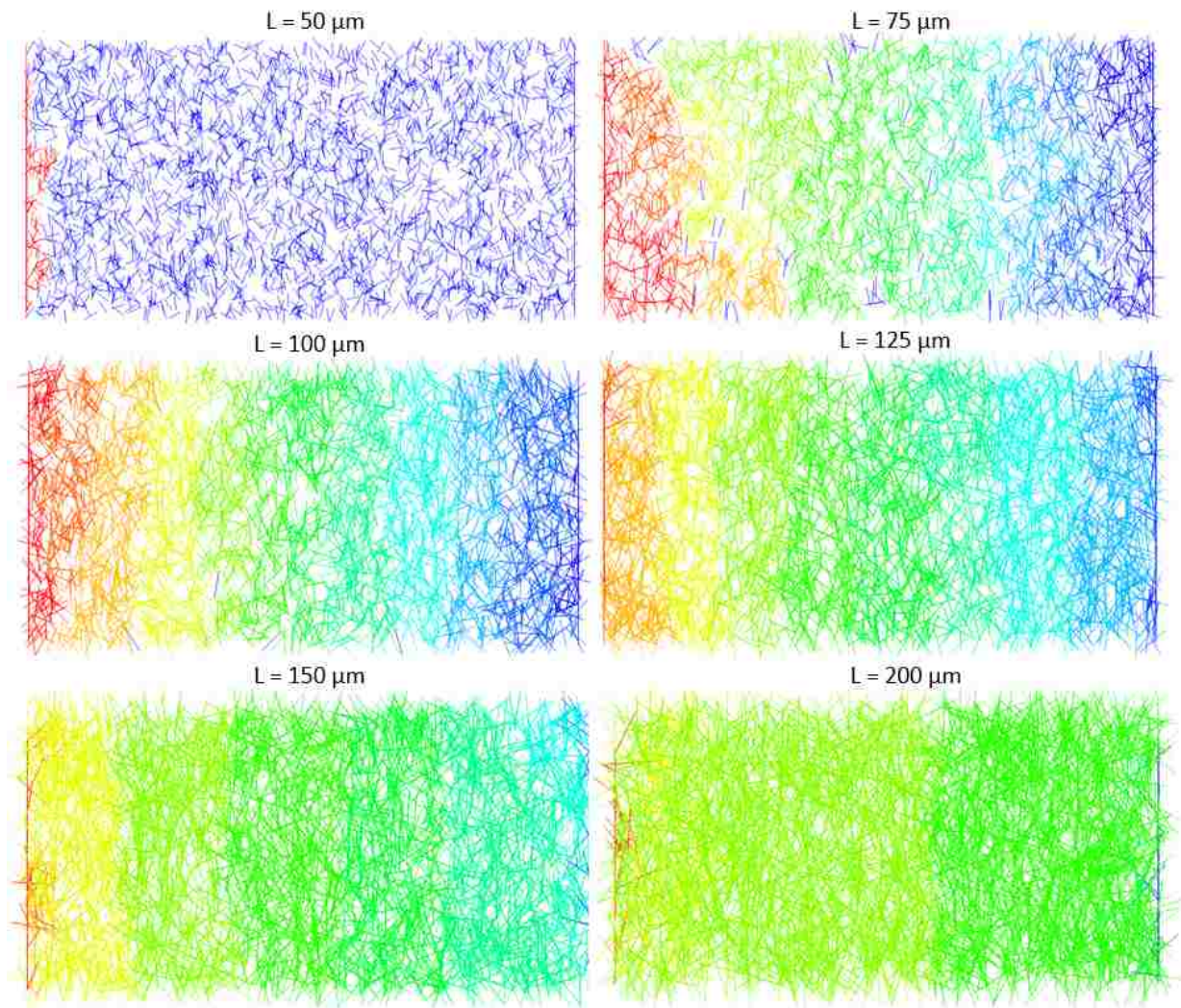


Figure 5.10: Voltage Contours for Increasing Fiber Lengths

An increasing trend in network conductivity can be observed in Figure 5.11 for increasing fiber lengths as it is now easier for the network to bridge the gap between electrodes.

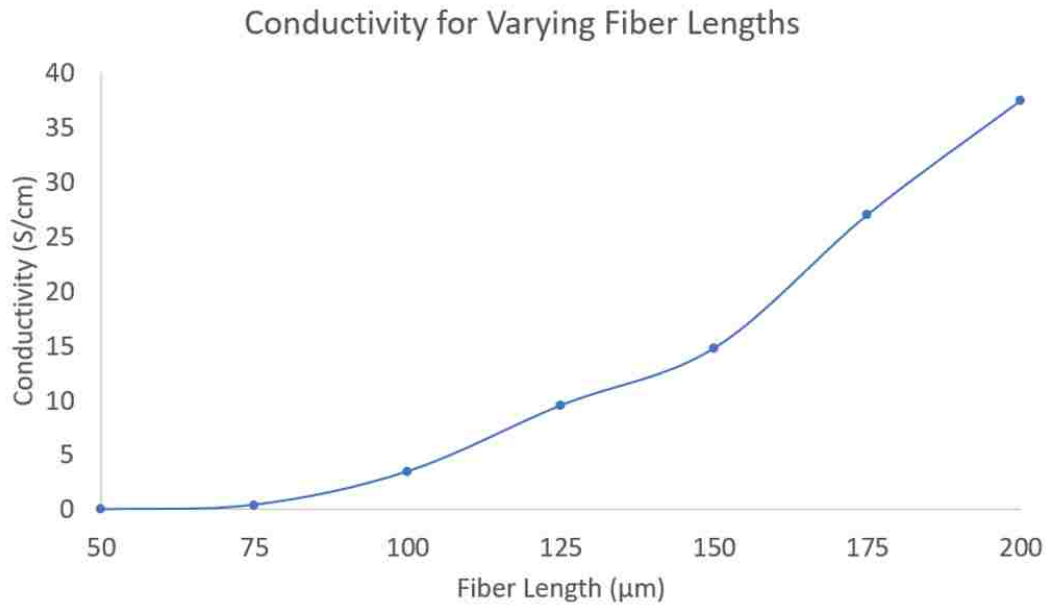


Figure 5.11: Conductivity Changes for Varying Fiber Lengths

5.2.2 Tunneling Parameters

As previously discussed, the energy barrier height and tunneling thickness significantly affect tunneling; and in turn, composite conductivity. Since several energy barrier height values are reported in literature (3.3 - 3.8 eV) [23, 45, 46, 47, 48, 70, 71, 72], the median of 3.55 eV was selected for this study. However, to illustrate the importance of this parameter, several simulations were conducted for various values in the stated range. Since this polymer does not shrink upon curing, the tunneling shell is assumed to remain at 1 nm for all cases. 3000 fibers with 100 μm lengths and 200 nm diameters were the other fixed parameters. Figure 5.12 indicates small variations in network conductivity for varying energy barrier heights. The median value of 3.55 eV is a good representation for the manufactured composite.

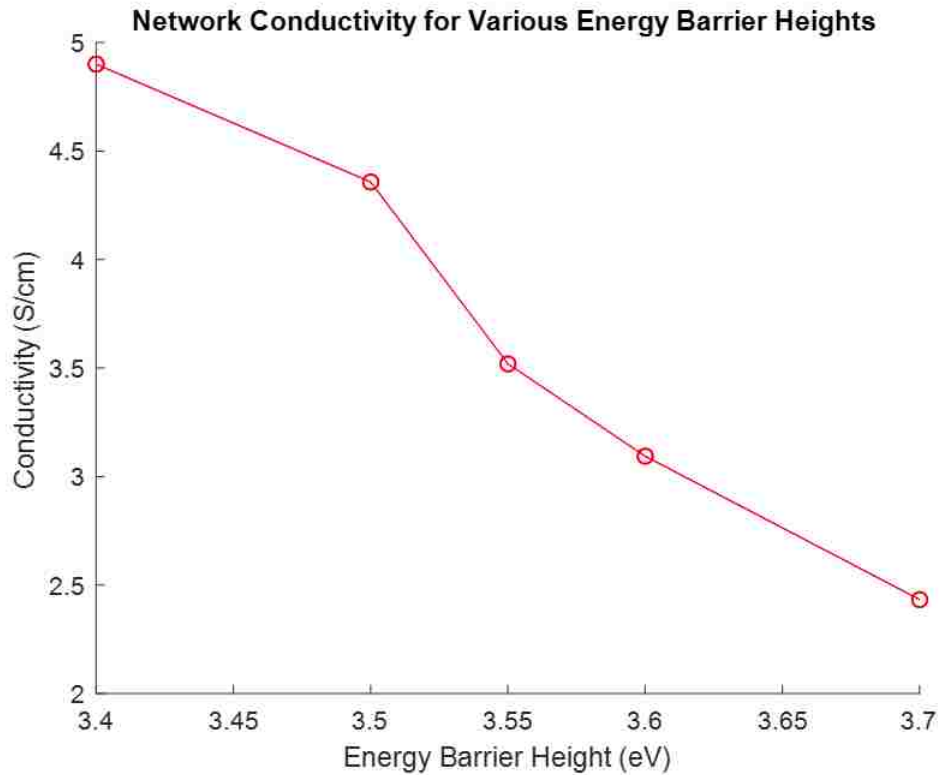


Figure 5.12: Conductivity Changes for Varying Energy Barrier Heights

The two parameters directly stated in the input file are fiber cross-sectional area and network tunneling conductivity. The calculation of tunneling conductivity is made with the stated values for energy barrier height and tunneling shell. The tunneling distance of 1 nm is typical for the type of carbon nanopaper used in the experimental study. This value is deemed acceptable for the model and is verified experimentally. 3000 fibers with lengths of 100 μm and diameters of 200 nm, and an energy barrier height of 3.55 eV were the fixed parameters. The tunneling conductivity at a single junction is 2.45×10^{-6} S/cm for the stated parameters. The number of junctions is calculated for each simulation and multiplied by the tunneling conductivity. The average tunneling conductivity is 0.0314 S/cm. Figure 5.13 is a histogram of the number of junctions from 40 simulations. The average number of junctions for 3000 fibers is 12818. A positive skewness can be observed.

Monte Carlo simulations run hundreds to thousands of simulations. A more Gaussian distribution is expected as the number of simulations increases. The tunneling conductivity changes minimally for the range of number of junctions. It is 0.0307 S/cm for the lowest number of junctions and 0.0325 S/cm for the highest.

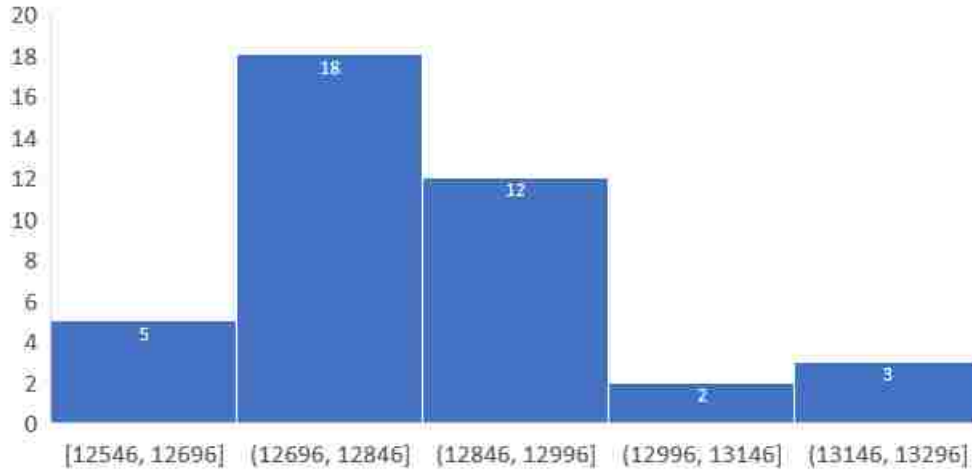


Figure 5.13: Number of Junctions Histogram

Recalling the equation for the tunneling shell,

$$t_0 = \frac{h}{4\pi\sqrt{2m_e\lambda}} W\left(\frac{2^9 q_e^2 l_{CNF} m_e v_f \rho_0 \lambda}{h^3 \pi^4}\right) \quad (5.17)$$

The experimentally measured resistivity can be used to verify the value of 1 nm found in literature. Solving the equation above outputs a value of 1.01 nm for the fabricated composite. A value of 1 nm was therefore deemed acceptable and used for all other simulations.

Figure 5.14 illustrates how composite conductivity changes with tunneling thickness. The energy barrier height of 3.55 eV is assumed for all cases. Network conductivity can be seen to be extremely sensitive to the tunneling shell value.

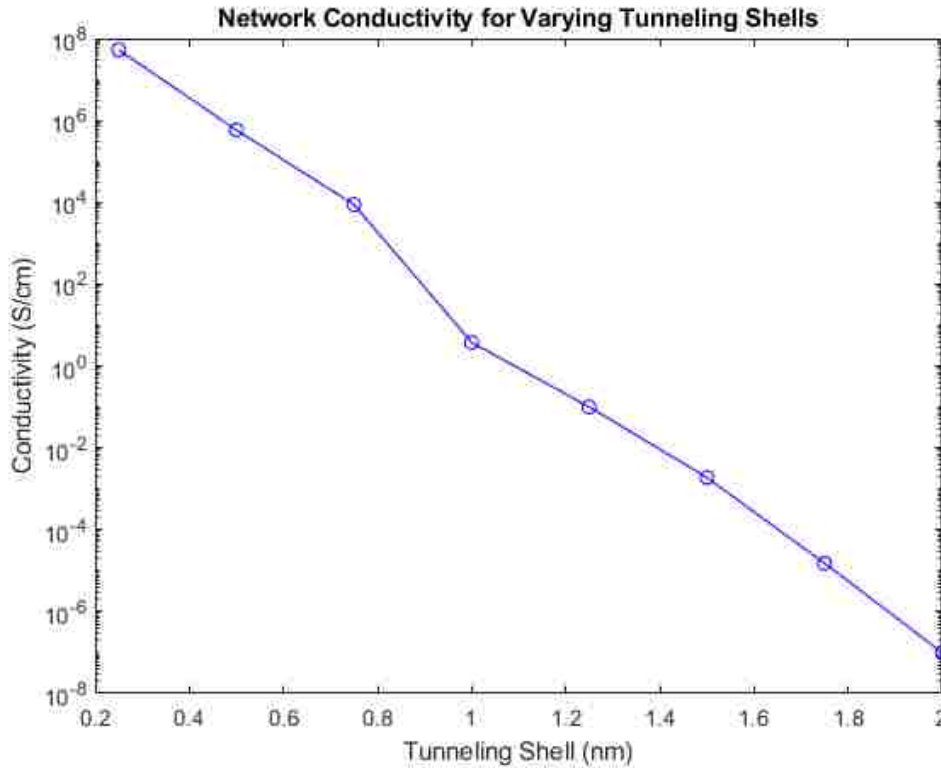


Figure 5.14: Composite Conductivity Changes for Varying Tunneling Shells

5.2.3 Voltage Variations

An electrical potential of 10 V was originally selected as a common voltage value for strain sensing. Variations in this value were assessed to ensure that the network conductivity results did not change. Figure 5.15 displays the voltage contours for 10, 20 and 30 V respectively. 3000 fibers with lengths of $100 \mu\text{m}$ and diameters of 200 nm, tunneling shell of 1 nm and energy barrier height of 3.55 eV were the fixed parameters. A minimal change in conductivity was observed for these variations. The network conductivity average for all three cases was 3.57 S/cm with a standard deviation of 0.263.

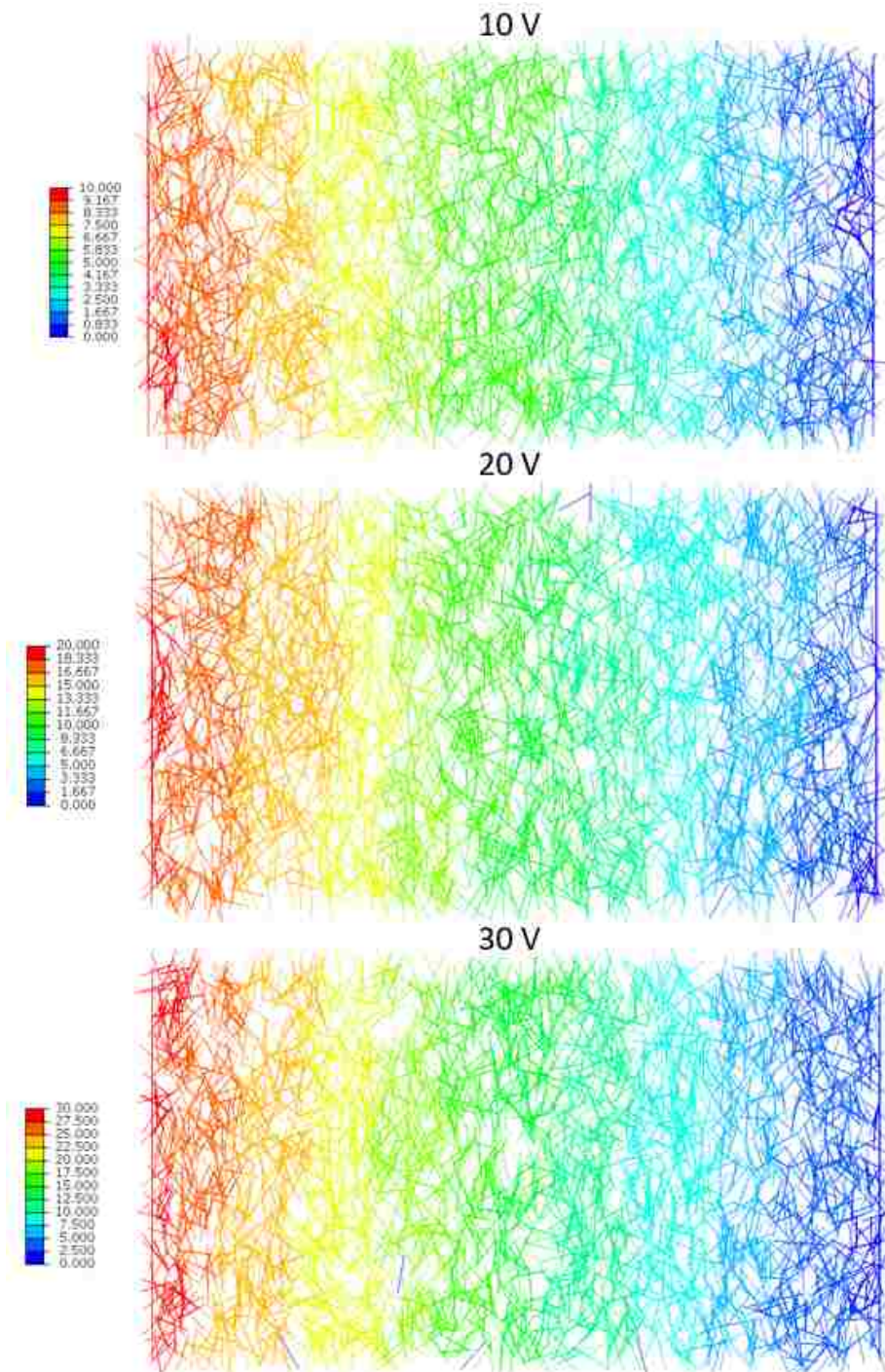


Figure 5.15: Voltage Variations

5.3 Model Results

With the sensitivity study of input parameters complete, the final model simulations can be run. Table 5.2 presents the values decided upon after the sensitivity study that best represent the manufactured composite.

Table 5.2: Simulation Input Parameters

Fibers	Diameter	200 nm
	Length	100 μm
	Cross-Sectional Area	3.142e-10 cm^2
	Number of Fibers	3000
	Tunneling Conductivity	0.03 S/cm
Matrix	Poisson's Ratio	0.47
	Energy Barrier Height	3.55 eV
	Insulator Thickness	1 nm
FEA	Electrical Potential	10 V
	Unit Cell (L x W)	2 x 1 mm
	Strain	2%

Contour plots for current density and voltage are first presented for the initial state in Figure 5.16. The electron paths can be observed in the current density contour. Fibers that contribute minimally to the flow of current are blue. It is common for dense networks that several paths lead to one junction at some location. This results in a significantly higher current density as that junction is one of only a few pathway gates between electrodes. It is for this reason that the legend is scaled to better visualize the pathways between electrodes for the predominantly lower current densities. While the current summation provides the desired parameter, these plots illustrate the current paths that electrons take.

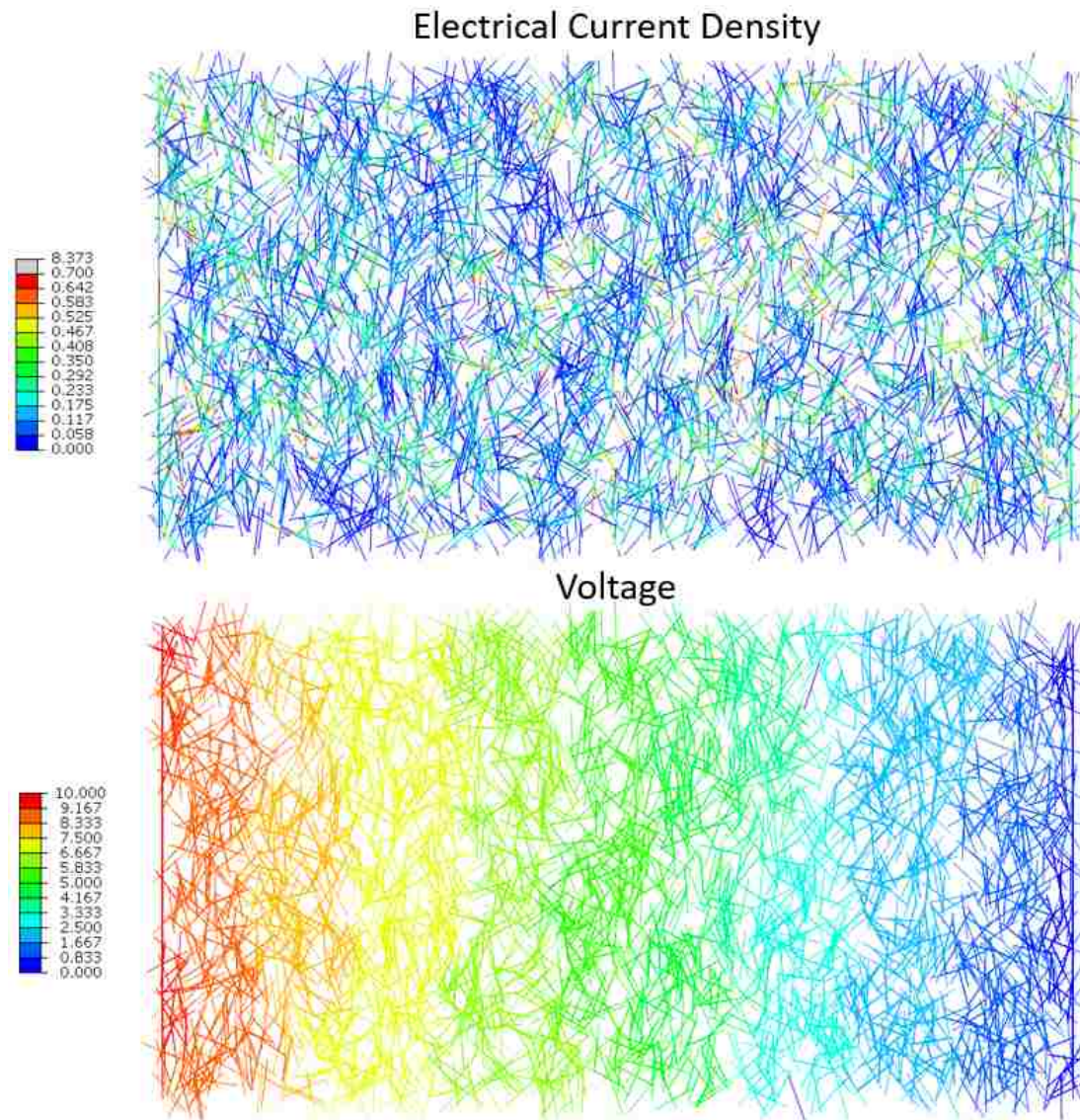


Figure 5.16: Current Density and Voltage Contours for Initial Network State

Input files for the initial and deformed states are generated at the same time. Each deformation case is now solved. The following plots show a small decrease in current density under a 2% strain. The current density and voltage contour plots are presented in Figure 5.17. The voltage plot for the initial state is displayed. There is no change in voltage distribution for a deformed network.

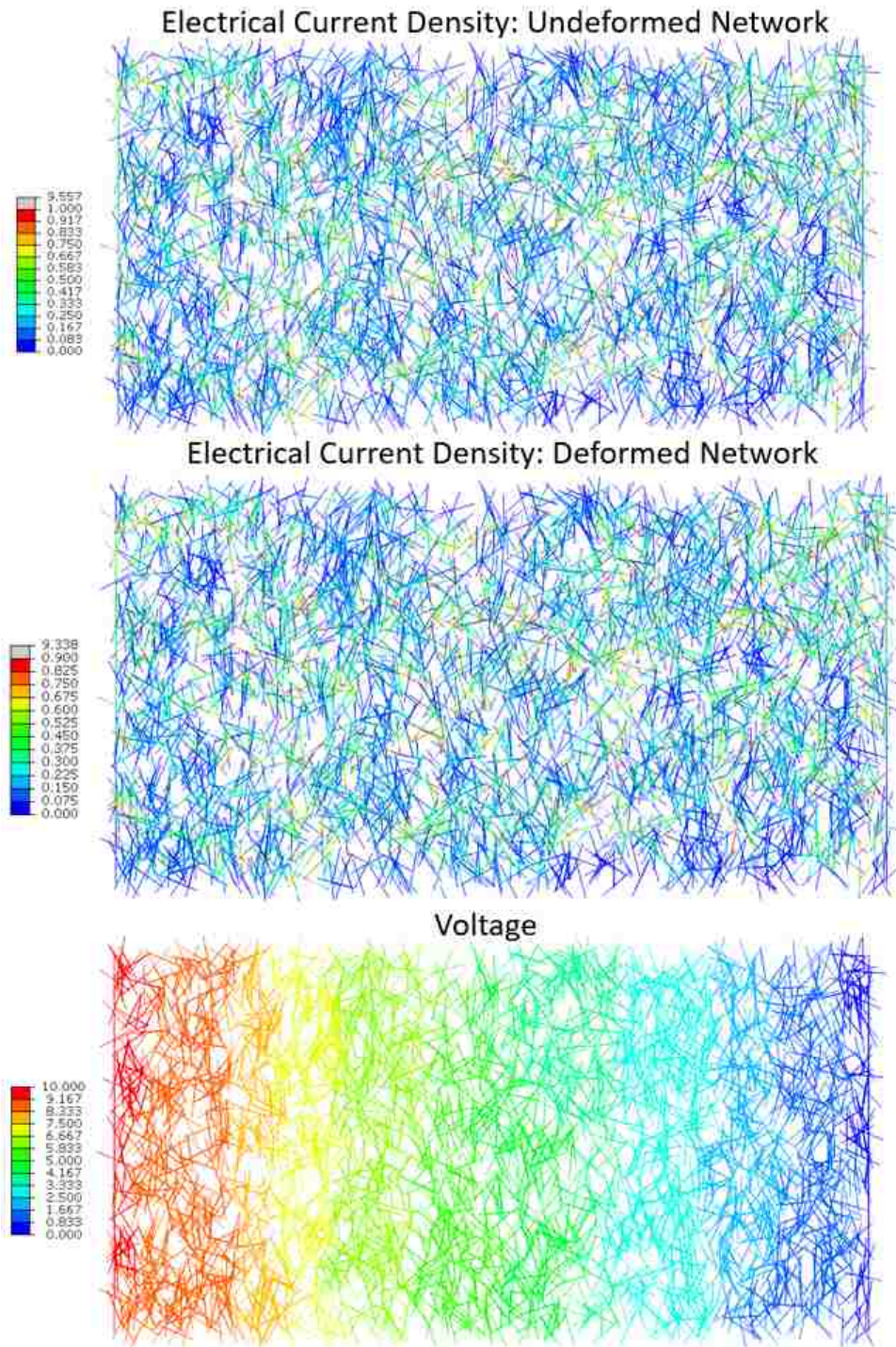


Figure 5.17: Piezoresistive Current Density and Voltage Contours at 2% Strain

Since the path required for current to flow is now longer, resistance increases. Additionally, some junctions break causing a larger resistance increase. However, at very low strains, the number of broken junctions is very small. For dense networks, new junctions can also form when old ones break. A good piezoresistive behavior is best captured for highly stretchable composites when high strains are involved for a filler concentration at the percolation threshold. Model results in Table 5.3 show the expected decrease in conductivity for the deformed state.

Table 5.3: Model Conductivity and Piezoresistivity Results

Measure	Average
Initial State Conductivity (S/cm)	3.365 ± 0.529
Deformed State Conductivity (S/cm)	3.115 ± 0.489
Relative Resistance Change	0.074 ± 0.033
Gauge Factor	3.72 ± 1.66

The relative resistance change is quite low. A large change indicates better strain sensitivity. While sparse networks may have a lower conductivity, they tend to have a higher piezoresistivity. Fiber aspect ratio and filler volume fraction have a similar effect on conductivity and piezoresistivity [73]. A higher piezoresistivity can be attained with lower fiber aspect ratios and intrinsic resistances. Furthermore, fibers that are aligned greatly improve piezoresistive performance.

CHAPTER 6: RESULTS DISCUSSION

6.1 Experimental and Model Results Comparison

Table 6.1 results show that initial state conductivity is predicted relatively well but piezoresistivity is underpredicted. The piezoresistive behavior is underpredicted in this model due to deformation only occurring in two dimensions, and tunneling conductivity being assumed at all junctions. Although the error percentage is high for the piezoresistive characteristics, the model does capture the governing behavior. This error will drop significantly when the network is modeled in 3D.

Table 6.1: Model and Experimental Results Comparison

Measure	Model	Experiment	% Error
Conductivity (S/cm)	3.365 ± 0.529	4.047 ± 0.002	16.85
Relative Resistance Change at 2% Strain	0.074 ± 0.033	0.13 ± 0.016	43.08
Gauge Factor	3.72 ± 1.66	6.625 ± 0.82	43.85

Figure 6.1 simulated the relative resistance change in quarter intervals up to 2% strain. The model predicts better piezoresistivity at very low strains because there is a very small increase in resistance. In the higher regions, there is a drop off in sensitivity due to the model underestimating the breaking of junctions.

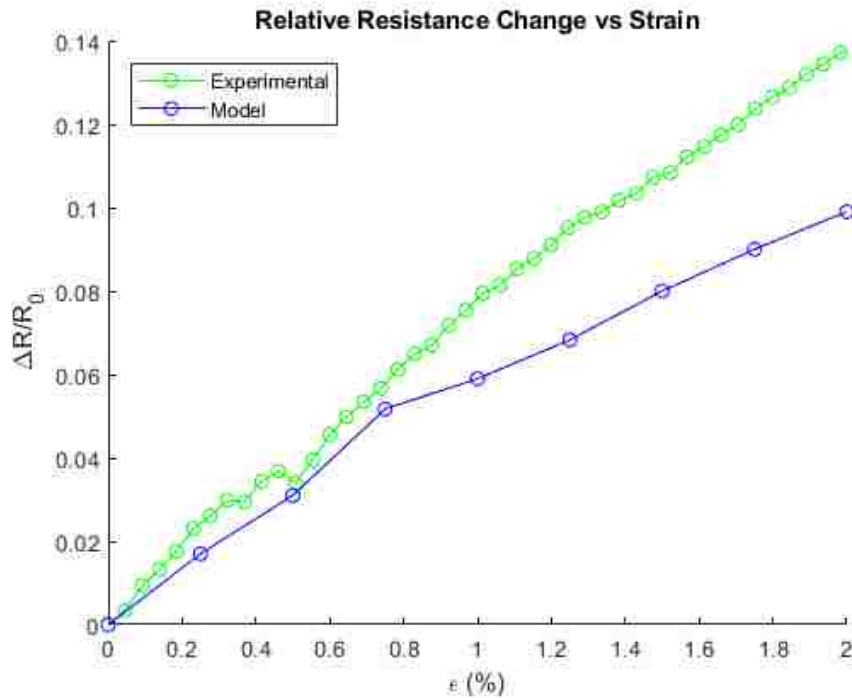


Figure 6.1: Model and Experimental Results Comparison

6.2 Model Limitations

First, this is a simple 2D model and will therefore underpredict piezoresistive response under a deformation because two fibers still create a junction at low strains. In 3D, fibers have an additional rotation which results in the more likely breaking of junctions. Furthermore, the tunneling shell distance will increase, significantly lowering conductivity. Although tunneling is considered in this model, an insulating thickness of 1 nm is assumed for all junctions. An improved model would calculate the shortest distance between two fibers and the corresponding tunneling resistance. This method, while more accurate, is significantly more computationally expensive as fibers will constantly have to be adjusted so as not to physically touch each other. Once that task is done, the various tunneling distances would need to be calculated and the conductive paths determined. A

resistor network model would solve for the representative volume element conductivity in a similar fashion to this model.

As discussed, this study provides an initial framework for a simple 2D percolation based conductivity model. It does not take into account 3D geometry, fiber waviness and agglomeration effects. Additionally, it does not consider variations in fiber lengths and diameters, which are quite significant (length: 30 - 100 μm , diameter: 60 - 200 nm). As such, it is expected to underpredict conductivity but within an acceptable range. Furthermore, the deformation equations are for unidirectional tensile cases and are simple in derivation. Actual fiber repositioning is difficult to model unless assuming rigid body motion.

The benefit of the MATLAB code written in this study is that it can be constantly improved to predict a more accurate strain response by expanding the representative volume element to 3D, accounting for agglomerations, fiber waviness and intrinsic resistance, and by better predicting tunneling. This model assumed tunneling at all junctions since the tunneling distance (1 nm) is significantly smaller than fiber diameter (200 nm). Further model developments will more accurately capture tunneling between adjacent fibers and consider intrinsic resistance. As such, this model underpredicts piezoresistivity because it assumes tunneling at all junctions. While this assumption is fine for simple models, a more developed one will produce a network with a higher conductivity and a better piezoresistivity because the tunneling resistance will decrease.

CHAPTER 7: CONCLUSION

7.1 Findings

A fast computational model was developed that can provide adequate predictions for initial state electrical conductivity and display voltage and electrical current density contours due to being used in conjunction with finite element analysis. The percolation threshold can be determined and the conductivity estimated to within acceptable tolerances. The piezoresistive behavior is underpredicted in this model due to deformation only occurring in two dimensions, and tunneling conductivity being assumed at all junctions. Additionally, simplified strain equations result in little to no junction breaks. Despite its 2D nature, the model captures the mechanism of piezoresistivity to a certain extent but underpredicts the relative resistance change. Experimental tests indicate that an effective composite capable of strain sensing can be fabricated inexpensively with simple processing techniques and have a gauge factor greater than traditional metallic strain sensors. Results display moderately good linearity and sensitivity for few cycles at low strains. High cycle tests revealed slight decreases in strain sensitivity with each subsequent cycle, hindering repeatability performance.

7.2 Future Work

The first next step would be to convert the developed model to three dimensions as illustrated in Figure 7.1. The current code already generates fibers with (x,y,z) coordinates, the z coordinates are just zero. The fiber intersection function will have to be updated as fibers now intersect a plane at the boundaries and not a line. Strain application will take into account an azimuthal angle in addition to the polar angle. This will provide a more accurate piezoresistive reading as discussed.

Additionally, a high number of Monte Carlo simulations will be run and a convergence study will be made to describe the effect of the representative volume element size and number of fibers on electrical conductivity.

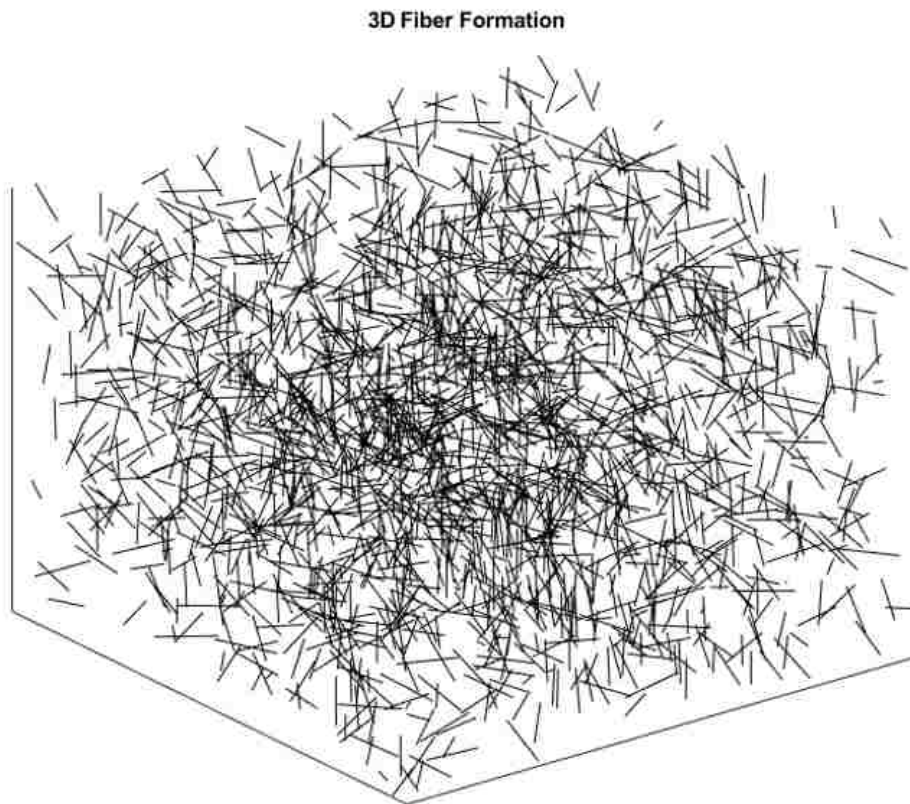


Figure 7.1: 3D Fiber Network

Li et al. [26] has shown by Monte Carlo simulations that wavy nanotube networks have a lower conductivity compared to straight nanotubes. Therefore, waviness and fiber clustering will be taken into account for model development to better predict conductivity. Panozzo et al. [50] introduced a coefficient of non-straightness. It is simply the ratio of the effective fiber length and its actual length. While this makes the model more accurate, it does require a significant amount of coding as now fibers can now intersect themselves. Furthermore, variations in fiber lengths and diameters

can be considered to add more randomness to the simulation.

A carbon nanomaterial based polymer nanocomposite has the potential to be a flexible, sensitive and stable strain sensor in addition to providing electrical heat actuation for the shape memory effect in polymers. Studies have shown that carbon nanomaterials exhibit excellent electric heating performance, are thermally stable at high temperatures, and are energy efficient at constant voltages [12]. Since sensing and heating capabilities both depend on the microstructure, they are coupled. This coupling mechanism is not well understood. Further studies seek to understand the interactions between electrical, thermal and mechanical properties of carbon nanomaterials and how the cracking of the conductive networks under different loads affect these properties. A model relating strain, electrical resistance and temperature is sought after, especially when the composite undergoes actuation. Factors like aspect ratio, volume fraction and conductivity of the carbon nanomaterials significantly affect the electric heating properties. By understanding the relationships between the material properties, both an effective strain sensor and heater can be designed.

APPENDIX A: MATLAB CODE

Main Code

First, the input parameters are set by the user. Next, four functions are called to perform certain tasks. Descriptions of these functions and the functions themselves follow after this main code section. A plot of the fiber formation is generated for visual confirmation before job submittal. Lastly, the ABAQUS input file is generated. The code labels which nodes comprise which elements, defines the source and drain electrodes as boundaries, applies an electric potential, specifies element type and assembles the mesh. Once the deformation is applied, the new x,y coordinates are rerun through the Fiber Intersection and Merge Nodes Functions and the new network conductivity is determined. A second input file is then generated for the deformed state. Since the deformation codes are nearly identical to the presented functions, they are omitted from this appendix.

```
%%%%%%%%%%%%%%%%%%%%%%%%%%%%%%%%%%%%%%%%%%%%%%%%%%%%%%%%%%%%%%%%%%%%%%%% Electrical Conductivity 2D Model Main Code %%%%%%%%%%%%%%%%%%%%%%%%%%%%%%%%%%%%%%%%%%%%%%%%%%%%%%%%%%%%%%%%%%%%%%%%%
clear all
clc
close all

% Input Parameters
% Unit Cell
a = ; % Unit Cell Width (cm)
b = ; % Unit Cell Height (cm)
% Fibers
dia = ; % Diameter (cm)
leng = ; % Length (cm)
CS = pi*(dia/2)^2; % Cross Sectional Area (cm^2)
N = ; % Number of Fibers
% Matrix
nu = ; % Poisson's Ratio
lambda = ; % Energy Barrier Height (eV)
```

```

t = ; % Tunneling Shell (cm)
% Physical Constants
me = 9.10938e-31; % Electron Mass (kg)
qe = 1.602e-19; % Electron Charge (C)
h = 6.626e-34; % Planck's Constant (m^2kg/s)
% Strain
epsilon = ;
% Voltage
V = ;

%% Generate Fibers and Electrodes
[x, y, z, xc, yc, theta] = FiberGeneration(leng, N, a, b);

%% Fiber Intersection
[x_intersect, y_intersect] = FindIntersection(x, y, N);

%% Merge Stacked Nodes
[x_full, y_full, numbering, pairs] = MergeNodes(x, y, x_intersect, y_intersect
, N);

%% Determine Tunneling Conductivity
num_junctions = nnz(x_intersect)/2; % Number of Junctions
Res_Tun_Junction = (h^2*t*1e-2)/(CS*1e-4*qe^2*sqrt(2*me*lambda*qe))*exp((4*pi*
t*1e-2)/h*sqrt(2*me*lambda*qe)); % Tunneling Resistance
Rho_Tun_Junction = Res_Tun_Junction*pi*((dia*1e-2)/2)^2/(t*1e-2); %
Tunneling Resistivity
sig_Tun_Junction = 1/(Rho_Tun_Junction*100); % Tunneling Conductivity at one
Junction S/cm
sig_Tun_Network = sig_Tun_Junction*num_junctions; % Tunneling Conductivity of
Fiber Network

```



```

%% Apply Deformation
[x_new, y_new] = AppliedStrain(dia, epsilon, x, y, nu, b);

%% Plot Fibers
figure (1);
plot(x(:,1),y(:,1),'r', 'Linewidth',2)
hold on
plot(x(:,2),y(:,2),'b', 'Linewidth',2)

for o = 3:length(x(1,:))
plot(x(:,o),y(:,o),'k', 'Linewidth',dia)
end

for o = 1:length(x_full(1,:))
scatter(x_full(:,o),y_full(:,o),'k', 'filled')
end
title('Fiber Formation')
xlim([-0.2*a 1.2*a])
ylim([-0.2*b 1.2*b])

%% Generate Input File
fileID = fopen('ConnectedFibers.txt','w');
fprintf(fileID, '*Heading\n** Job name: Initial Electrical Conductivity
Simulation \n** Model name: Generated Fibers\n');
fprintf(fileID, '** Generated by: Abaqus/Standard\n*Preprint, echo=NO, model=
NO, history=NO, contact=NO \n');
fprintf(fileID, '**\n** Base Unit: cm\n');
fprintf(fileID, '** Unit Cell \t%d,\t%d\n', a, b);
fprintf(fileID, '** Number of Fibers \t%d\n', N);
fprintf(fileID, '** Fiber Diameter \t%d\n', dia);
fprintf(fileID, '** Fiber Length \t%d\n', leng);

```

```

fprintf(fileID, '** Fiber Cross Sectional Area \%1d\n', CS);
fprintf(fileID, '** Energy Barrier Height \%1d\n', lambda);
fprintf(fileID, '** Insulator Thickness \%1d\n', t);
fprintf(fileID, '** Tunneling Conductivity \%1d\n', sig_Tun_Network);
fprintf(fileID, '** Number of Junctions \%1d\n', num_junctions);
fprintf(fileID, '** Electric Potential \%1d\n', V);
fprintf(fileID, '**\n** PARTS \n** \n*Part, name=Part-1 \n*Node \n');
k = 1;
generated_nodes = zeros(length(x_full(:,1)),length(x_full(1,:)));
for i = 1:N+2
    lim = nnz(x_full(:,i));
    for j = 1:lim
        if length(find(pairs(:,2) == k)) == 0
            fprintf(fileID, '\t%1d,\t%1d,\t%1d,\t0\n', k, x_full(j,i), y_full(j,i)
                );
            generated_nodes(j,i) = k;
        else
            loc = find(pairs(:,2) == k);
            generated_nodes(j,i) = pairs(loc,1);
        end
        k = k + 1;
    end
end
end
no_nodes = k - 1;

fprintf(fileID, '*Element, type=DC1D2E\n');

k = 1;
for i = 1:N+2
    lim = nnz(x_full(:,i));
    for j = 1:lim-1

```

```

        fprintf(fileID, '\t%d,\t%d,\t%d\n', k, generated_nodes(j,i),
            generated_nodes(j+1,i));
        k = k + 1;
    end
end
no_elements = k - 1;
fprintf(fileID, '*Nset, nset=Set-1, generate\n');
fprintf(fileID, '\t1,\t%d,\t1\n', no_nodes);
fprintf(fileID, '*Elset, elset=Set-1, generate\n');
fprintf(fileID, '\t1,\t%d,\t1\n', no_elements);
fprintf(fileID, '** Section: Section-1\n*Solid Section, elset=Set-1, material=
    Material-1\n\t%d,\n*End Part\n**\n**\n', CS);
fprintf(fileID, '** ASSEMBLY\n**\n*Assembly, name=Assembly\n**\n*Instance, name
    =Part-1-1, part=Part-1\n*End Instance\n**\n');

fprintf(fileID, '*Nset, nset=Source, instance=Part-1-1\n');
fprintf(fileID, ' 1');
for j = 2:nz(x_full(:,1))
    fprintf(fileID, ',\t%d', j);
end

fprintf(fileID, '\n*Elset, elset=Source, instance=Part-1-1\n');
fprintf(fileID, ' 1');
for j = 2:nz(x_full(:,1))-1
    fprintf(fileID, ',\t%d', j);
end

fprintf(fileID, '\n*Nset, nset=Drain, instance=Part-1-1\n');
fprintf(fileID, ' %d', nz(x_full(:,1)) + 1);
for j = nz(x_full(:,1)) + 2:nz(x_full(:,1)) + nz(x_full(:,2))
    fprintf(fileID, ',\t%d', j);

```

```

end
fprintf(fileID, '\n*Elset, elset=Drain, instance=Part-1-1\n');
fprintf(fileID, ' %d', nnz(x_full(:,1)));
for j = nnz(x_full(:,1)) + 1:nnz(x_full(:,1)) + nnz(x_full(:,2))-2
    fprintf(fileID, ',\t%d', j);
end
fprintf(fileID, '\n*End Assembly\n**\n');
fprintf(fileID, '** MATERIALS\n**\n*Material, name=Material-1\n*Electrical
    Conductivity\n\t%d,\n', sig_Tun_Network);
fprintf(fileID, '**
    -----\n**\n**
    STEP: Step-1\n**\n*Step, name=Step-1, nlgeom=NO\n*Coupled Thermal-
    electrical, steady state, deltmx=0.\n0.001, 1., 1e-05, 1.,\n**\n');
fprintf(fileID, '** BOUNDARY CONDITIONS\n**\n** Name: BC-1 Type: Electric
    potential\n*Boundary\nSource, 9, 9, 10.\n** Name: BC-2 Type: Electric
    potential\n*Boundary\nDrain, 9, 9\n');
fprintf(fileID, '**\n** OUTPUT REQUESTS\n**\n*Restart, write, frequency=0\n**\n
    ** FIELD OUTPUT: F-Output-1\n**\n*Output, field\n*Node Output\nEPOT,\n*
    Element Output, directions=YES\nECD, EPG\n*Contact Output\nECD, ECDA\n**\n
    ** HISTORY OUTPUT: H-Output-1\n**\n*Output, history, variable=PRESELECT\n*
    End Step\n');
fclose(fileID);

```

Microstructure Generation Function

The source and drain electrode boundaries are first created followed by the generation of randomly oriented fibers. This is achieved through complex analysis where the real part provides the x coordinates and the imaginary part provides the y coordinates. Fibers are generated with nodes at the endpoints, beginning the mesh generation process.

```
function [x, y, z, xc, yc, theta] = FiberGeneration(leng, N, a, b)

% Source Electrode
xc_source = 0;
yc_source = b/2;
theta_source = pi/2;

u = 1;
for j = -1:2:1
    z(u,1) = xc_source + i*yc_source + j*b*exp(i*theta_source)/2;
    u = u + 1;
end

% Drain Electrode
xc_drain = a;
yc_drain = b/2;
theta_drain = pi/2;

u = 1;
for j = -1:2:1
    z(u,2) = xc_drain + i*yc_drain + j*b*exp(i*theta_drain)/2;
    u = u + 1;
end
```

```

% Randomly Oriented Fibers
for k = 1:N
    xc = a*rand(1,N);
    yc = b*rand(1,N);
    theta = asin(1-2*rand(1,N)) + pi/2;
    u = 1;
    for j = -1:2:1
        z(u,k+2) = xc(k) + yc(k)*i + j*leng*exp(-i*theta(k))/2;
        u = u + 1;
    end
end

x = real(z);           % x Coordinates
y = imag(z);          % y Coordinates
end

```

Find Intersection Function

The intersection points between fibers and the electrodes are then determined using a method of determinants. The starting (x_1, y_1) and ending coordinates (x_2, y_2) are first identified in the generation matrix. The MATLAB end command is used to determine the last coordinate. A conditional statement is applied to ensure that the intersection point being recorded is on the fiber length and not at a point beyond the two lines. A small del increment is used to help restore some lost accuracy in the fiber generation process. With this accuracy restored, boundary intersection points can be determined.

```

function [x_intersect, y_intersect] = FindIntersection(x, y, N)

for j = 1:N+2
    for i = 1:N+2
        x1 = x(1,j); y1 = y(1,j); x2 = x(end,j); y2 = y(end,j);           %
        Components of Line 1
        if i == j
            x_intersect(i,j) = 0;
            y_intersect(i,j) = 0;
        else
            x3 = x(1,i); y3 = y(1,i); x4 = x(end,i); y4 = y(end,i);       %
            Components of Line 2

            x_intersect(i,j) = det([det([x1 y1;x2 y2]), (x1-x2);det([x3 y3;x4
                y4]), (x3-x4) ])/det([(x1-x2), (y1-y2); (x3-x4), (y3-y4)]);
            y_intersect(i,j) = det([det([x1 y1;x2 y2]), (y1-y2);det([x3 y3;x4
                y4]), (y3-y4) ])/det([(x1-x2), (y1-y2); (x3-x4), (y3-y4)]);

            xlow1 = min(x1,x2);
            xhigh1 = max(x1,x2);
            ylow1 = min(y1,y2);
            yhigh1 = max(y1,y2);

            xlow2 = min(x3,x4);
            xhigh2 = max(x3,x4);
            ylow2 = min(y3,y4);
            yhigh2 = max(y3,y4);

            del = 1e-16;
            if x_intersect(i,j) <= xhigh1 + del && x_intersect(i,j) >= xlow1 -
                del && y_intersect(i,j) <= yhigh1 + del && y_intersect(i,j)

```

```

>= ylow1 - del
    if x_intersect(i,j) <= xhigh2 + del && x_intersect(i,j) >=
        xlow2 - del && y_intersect(i,j) <= yhigh2 + del &&
            y_intersect(i,j) >= ylow2 - del
            x_intersect(i,j) = x_intersect(i,j) + del;
            y_intersect(i,j) = y_intersect(i,j) + del;
        else
            x_intersect(i,j) = 0;
            y_intersect(i,j) = 0;
        end
    else
        x_intersect(i,j) = 0;
        y_intersect(i,j) = 0;
    end
end
end
end
end
end
end
end

```

Merge Nodes Function

In order for current to flow through the resistor network in FEA analysis, fiber intersection points need to share one node. Since the mesh was created during the fiber generation process, nodes may not be located at this point. Once the intersection points are found, a node is placed there. However, since a pair of fibers share an intersection point, two stacked nodes are created. This function constructs a matrix of the fiber pairs that share nodes and deletes the stacked one.


```

function [x_full, y_full, numbering, pairs] = MergeNodes(x, y, x_intersect,
    y_intersect, N)

max_dim = nnz(x_intersect(:,1));

for i = 2:N+2
    temp = nnz(x_intersect(:,i));
    if temp > max_dim
        max_dim = temp;
    end
end

x_full = zeros(max_dim + 2, N + 2);
y_full = zeros(max_dim + 2, N + 2);

for i = 1:N+2
    o(:,1) = nonzeros(x_intersect(:,i));
    o(:,2) = nonzeros(y_intersect(:,i));
    for j = 1:2+length(o(:,1))
        x_full(:,i) = [x(1,i); o(:,1); x(2,i); zeros(length(x_full(:,1))-2-
            length(o(:,1)),1)];
        y_full(:,i) = [y(1,i); o(:,2); y(2,i); zeros(length(y_full(:,1))-2-
            length(o(:,2)),1)];
    end
    clear o
end

o = 2;
for i = 1:N+2
    for j = 1:N+2
        if x_intersect(j,i) ~= 0

```

```

        numbering(j,i) = o;
        o = o + 1;
    else
        numbering(j,i) = 0;
    end
end
end
o = o + 2;
end

l = 1;
for i = 1:N+2
    for j = i:N+2
        if x_intersect(j,i) ~= 0
            pairs(l,1) = numbering(j,i);
            pairs(l,2) = numbering(i,j);
            l = l + 1;
        end
    end
end
end

end

```

Applied Strain Function

This function simply updates fiber positions and orientations for an applied strain. The new x,y coordinates are then rerun through the Find Intersection and Merge Nodes Functions, the new network conductivity is determined, and a second input file is written. Since these codes are identical to the ones presented with the exception that x,y become x_{new}, y_{new} , the codes are omitted.

```

function [x_new, y_new] = AppliedStrain(dia, epsilon, x, y, nu, b)

for m = 1:length(x(1,:))
    for n = 1:length(x(:,1))
        x_new(n,m) = x(n,m)*(1 + epsilon);
        y_new(n,m) = y(n,m) - nu*epsilon*(y(n,m) - b/2);
    end
end

%% Plot Deformed Fibers
figure (1);
plot(x_new(:,1),y_new(:,1),'r','Linewidth', dia)
plot(x_new(:,2),y_new(:,2),'b','Linewidth', dia)
hold on

for o = 2:length(x_new(1,:))
    plot(x_new(:,o),y_new(:,o),'g','Linewidth', dia)
end

for o = 1:length(x_new(1,:))
    plot(x_new(:,o),y_new(:,o),'g*','Linewidth', dia)
end
title('Deformed Fibers')
end

```

APPENDIX B: ABAQUS INPUT FILE

The following ABAQUS input file is for a simple case of 5 fibers. The node section indicates node number and x,y,z coordinates. The element section indicates which nodes make up each element. Node and element sets are created for the source and drain electrodes which are generated first and have an electric potential applied. Fiber cross-sectional area and electrical conductivity are assigned. Field outputs are electric potential and electrical current density.

```
*Heading
** Job name: Initial Electrical Conductivity Simulation
** Model name: Generated Fibers
** Generated by: Abaqus/Standard
*Preprint, echo=NO, model=NO, history=NO, contact=NO
**
** Base Unit: cm
** Unit Cell    1.000000e-02,    1.000000e-02
** Number of Fibers      5
** Fiber Diameter    2.000000e-05
** Fiber Length      1.000000e-02
** Fiber Cross Sectional Area    3.141593e-10
** Energy Barrier Height      4
** Insulator Thickness    1.000000e-07
** Tunneling Conductivity    6.369099e-05
** Number of Junctions      8
** Electric Potential      10
**
** PARTS
**
*Part, name=Part-1
*Node
    1,  0,  0,  0
```

2,	0,	8.766203e-03,	0
3,	0,	1.000000e-02,	0
4,	1.000000e-02,	0,	0
5,	1.000000e-02,	5.407535e-03,	0
6,	1.000000e-02,	3.421964e-03,	0
7,	1.000000e-02,	1.000000e-02,	0
8,	1.842645e-03,	1.084726e-02,	0
10,	6.903629e-03,	7.472347e-03,	0
11,	1.016245e-02,	5.299206e-03,	0
12,	7.371548e-03,	1.009973e-02,	0
14,	6.667993e-03,	6.149241e-03,	0
15,	6.535804e-03,	5.406996e-03,	0
16,	5.618204e-03,	2.546382e-04,	0
17,	-3.826804e-03,	9.898316e-03,	0
19,	5.435248e-03,	7.158253e-03,	0
20,	5.762375e-03,	7.061476e-03,	0
21,	2.714765e-03,	9.384992e-03,	0
25,	6.860469e-03,	5.991697e-03,	0
26,	1.045310e-02,	3.051099e-03,	0
27,	7.043796e-03,	6.321857e-03,	0
30,	2.189297e-03,	-2.420788e-03,	0

*Element, type=DC1D2E

1,	1,	2
2,	2,	3
3,	4,	5
4,	5,	6
5,	6,	7
6,	8,	5
7,	5,	10
8,	10,	11
9,	12,	10

```

10, 10, 14
11, 14, 15
12, 15, 16
13, 17, 2
14, 2, 19
15, 19, 20
16, 21, 6
17, 6, 14
18, 14, 19
19, 19, 25
20, 25, 26
21, 27, 15
22, 15, 25
23, 25, 30

*Nset, nset=Set-1, generate
1, 30, 1

*Elset, elset=Set-1, generate
1, 23, 1

** Section: Section-1

*Solid Section, elset=Set-1, material=Material-1
3.141593e-10,

*End Part

**
**

** ASSEMBLY

**

*Assembly, name=Assembly

**

*Instance, name=Part-1-1, part=Part-1

*End Instance

**

```

```

*Nset, nset=Source, instance=Part-1-1
  1, 2, 3
*Elset, elset=Source, instance=Part-1-1
  1, 2
*Nset, nset=Drain, instance=Part-1-1
  4, 5, 6, 7
*Elset, elset=Drain, instance=Part-1-1
  3, 4, 5
*End Assembly
**
** MATERIALS
**
*Material, name=Material-1
*Electrical Conductivity
  6.369099e-05,
** -----
**
** STEP: Step-1
**
*Step, name=Step-1, nlgeom=NO
*Coupled Thermal-electrical, steady state, deltmx=0.
0.001, 1., 1e-05, 1.,
**
** BOUNDARY CONDITIONS
**
** Name: BC-1 Type: Electric potential
*Boundary
Source, 9, 9, 10.
** Name: BC-2 Type: Electric potential
*Boundary
Drain, 9, 9

```



```
**
** OUTPUT REQUESTS
**
*Restart, write, frequency=0
**
** FIELD OUTPUT: F-Output-1
**
*Output, field
*Node Output
EPOT,
*Element Output, directions=YES
ECD, EPG
*Contact Output
ECD, ECDA
**
** HISTORY OUTPUT: H-Output-1
**
*Output, history, variable=PRESELECT
*End Step
```

LIST OF REFERENCES

- [1] M. H. Al-Saleh and U. Sundararaj, "Review of the mechanical properties of carbon nanofiber/polymer composites," *Composites Part A: Applied Science and Manufacturing*, vol. 42, pp. 2126–2142, Dec. 2011.
- [2] S. Gong, Z. Zhu, and S. Meguid, "Carbon nanotube agglomeration effect on piezoresistivity of polymer nanocomposites," *Polymer*, vol. 55, pp. 5488–5499, Oct. 2014.
- [3] H. Lu, Y. Liu, J. J. Gou, J. Leng, and S. Du, "Surface coating of multi-walled carbon nanotube nanopaper on shape-memory polymer for multifunctionalization," *Composites Science and Technology*, vol. 71, pp. 1427–1434, July 2011.
- [4] "Nasa-isro synthetic aperture radar (nisar), nasa jet propulsion laboratory." <https://www.jpl.nasa.gov/missions/nasa-isro-synthetic-aperture-radar-nisar/>.
- [5] K. Suzuki, K. Yataka, Y. Okumiya, S. Sakakibara, K. Sako, H. Mimura, and Y. Inoue, "Rapid-response, widely stretchable sensor of aligned MWCNT/elastomer composites for human motion detection," *ACS Sensors*, vol. 1, pp. 817–825, June 2016.
- [6] "Spanwise adaptive wing, nasa glenn research center." <https://technology.nasa.gov/patent/LEW-TOPS-124>.
- [7] "Carbon nanotube based sensors, nasa langley research center." <https://technology.nasa.gov/>.
- [8] V. B. Ozdemir and K. Kwok, "Shape recovery behavior of carbon nanopaper shape memory polymer composite," in *AIAA Scitech 2019 Forum*, (San Diego, California), American Institute of Aeronautics and Astronautics, Jan. 2019.

- [9] H. Lu, F. Liang, Y. Yao, J. Gou, and D. Hui, "Self-assembled multi-layered carbon nanofiber nanopaper for significantly improving electrical actuation of shape memory polymer nanocomposite," *Composites Part B: Engineering*, vol. 59, pp. 191–195, Mar. 2014.
- [10] H. Lu, Y. Liu, J. Gou, and J. Leng, "Fabrication and properties of shape-memory polymer coated with conductive nanofiber paper," (Weihai, China), p. 749341, July 2009.
- [11] H. Lu, Y. Liu, J. Gou, J. Leng, and S. Du, "Electroactive shape-memory polymer nanocomposites incorporating carbon nanofiber paper," *International Journal of Smart and Nano Materials*, vol. 1, pp. 2–12, Feb. 2010.
- [12] J. Yan and Y. G. Jeong, "Multiwalled carbon nanotube/polydimethylsiloxane composite films as high performance flexible electric heating elements," *Applied Physics Letters*, vol. 105, p. 051907, Aug. 2014.
- [13] J. Gou, S. O'Braint, H. Gu, and G. Song, "Development and characterization of carbon nanopaper-based nanocomposite materials," in *Smart Structures and Materials 2006: Active Materials: Behavior and Mechanics* (W. D. Armstrong, ed.), vol. 6170, pp. 442 – 450, International Society for Optics and Photonics, SPIE, 2006.
- [14] J. Gou, J. Zhuge, F. Liang, R.-H. Chen, C. Ibeh, and D. Hui, "Carbon nanopaper enabled structural and multifunctional nanocomposites," *World Journal of Engineering*, p. 5, 2014.
- [15] M. Zhang, *Carbon nanomaterials for biomedical applications*. No. 10955 in Springer series in biomaterials science and engineering, New York, NY: Springer Science+Business Media, 1st ed., 2015.
- [16] X. Wang, J. Li, H. Song, H. Huang, and J. Gou, "Highly stretchable and wearable strain sensor based on printable carbon nanotube layers/polydimethylsiloxane composites with adjustable sensitivity," *ACS Applied Materials & Interfaces*, vol. 10, pp. 7371–7380, Feb. 2018.

- [17] J. H. Kim, J.-Y. Hwang, H. R. Hwang, H. S. Kim, J. H. Lee, J.-W. Seo, U. S. Shin, and S.-H. Lee, "Simple and cost-effective method of highly conductive and elastic carbon nanotube/polydimethylsiloxane composite for wearable electronics," *Scientific Reports*, vol. 8, Dec. 2018.
- [18] T. Tallman, S. Gungor, K. Wang, and C. Bakis, "Tactile imaging and distributed strain sensing in highly flexible carbon nanofiber/polyurethane nanocomposites," *Carbon*, vol. 95, pp. 485–493, 2015.
- [19] S. Wang, P. Xiao, Y. Liang, J. Zhang, Y. Huang, S. Wu, S.-W. Kuo, and T. Chen, "Network cracks-based wearable strain sensors for subtle and large strain detection of human motions," *Journal of Materials Chemistry C*, vol. 6, no. 19, pp. 5140–5147, 2018.
- [20] J. DeGraff, R. Liang, M. Q. Le, J.-F. Capsal, F. Ganet, and P.-J. Cottinet, "Printable low-cost and flexible carbon nanotube buckypaper motion sensors," *Materials & Design*, vol. 133, pp. 47–53, Nov. 2017.
- [21] F. Avils, A. I. Oliva-Avils, and M. Cen-Puc, "Piezoresistivity, strain, and damage self-sensing of polymer composites filled with carbon nanostructures," *Advanced Engineering Materials*, vol. 20, no. 7, p. 1701159, 2018.
- [22] T. Tallman, S. Gungor, G. Koo, and C. Bakis, "On the inverse determination of displacements, strains, and stresses in a carbon nanofiber/polyurethane nanocomposite from conductivity data obtained via electrical impedance tomography," *Journal of Intelligent Material Systems and Structures*, vol. 28, pp. 2617–2629, Nov. 2017.
- [23] Z.-M. Dang, M.-J. Jiang, D. Xie, S.-H. Yao, L.-Q. Zhang, and J. Bai, "Supersensitive linear piezoresistive property in carbon nanotube/silicone rubber nanocomposites," *Journal of Applied Physics*, vol. 104, no. 2, p. 024114, 2008.

- [24] M. Toms and S. Jalali, "Piezoresistivity in micro carbon fiber silicone composites for electrical resistance to strain sensing," *Advanced Engineering Forum*, vol. 23, pp. 45–55, July 2017.
- [25] A. Sanli, A. Benchirouf, C. Mller, and O. Kanoun, "Piezoresistive performance characterization of strain sensitive multi-walled carbon nanotube-epoxy nanocomposites," *Sensors and Actuators A: Physical*, vol. 254, pp. 61–68, Feb. 2017.
- [26] A. Li, A. E. Bogdanovich, and P. D. Bradford, "Aligned carbon nanotube sheet piezoresistive strain sensors," *Smart Materials and Structures*, vol. 24, p. 095004, Sept. 2015.
- [27] O. Kanoun, C. Mller, A. Benchirouf, A. Sanli, A. Bouhamed, A. Al-Hamry, and L. Bu, *Potential of Flexible Carbon Nanotube Films for High Performance Strain and Pressure Sensors*, pp. 148–183. 11 2014.
- [28] W. Obitayo and T. Liu, "A review: carbon nanotube-based piezoresistive strain sensors," *Journal of Sensors*, vol. 2012, pp. 1–15, 2012.
- [29] J. Bautista-Quijano, F. Avils, J. Cauich-Rodriguez, R. Schnfelder, A. Bachmatiuk, T. Gemming, and M. Rmmeli, "Tensile piezoresistivity and disruption of percolation in singlewall and multiwall carbon nanotube/polyurethane composites," *Synthetic Metals*, vol. 185-186, pp. 96–102, Dec. 2013.
- [30] S. M. Vemuru, R. Wahi, S. Nagarajaiah, and P. M. Ajayan, "Strain sensing using a multi-walled carbon nanotube film," *The Journal of Strain Analysis for Engineering Design*, vol. 44, pp. 555–562, Oct. 2009.
- [31] M. Rein, O. Breuer, and H. Wagner, "Sensors and sensitivity: carbon nanotube buckypaper films as strain sensing devices," *Composites Science and Technology*, vol. 71, pp. 373–381, Feb. 2011.

- [32] J. Zhu, S. Wei, J. Ryu, and Z. Guo, "Strain-sensing elastomer/carbon nanofiber metacomposites," *The Journal of Physical Chemistry C*, vol. 115, pp. 13215–13222, July 2011.
- [33] T. S. Natarajan, S. B. Eshwaran, K. W. Stckelhuber, S. Wiener, P. Ptschke, G. Heinrich, and A. Das, "Strong strain sensing performance of natural rubber nanocomposites," *ACS Applied Materials & Interfaces*, vol. 9, pp. 4860–4872, Feb. 2017.
- [34] H. Lu and J. Gou, "Significantly improving electromagnetic performance of nanopaper and its shape-memory nanocomposite by aligned carbon nanotubes," (San Diego, California), p. 834219, Apr. 2012.
- [35] H. Lu, F. Liang, J. (Jan) Gou, W. Min Huang, and J. Leng, "Synergistic effect of self-assembled carbon nanopaper and multi-layered interface on shape memory nanocomposite for high speed electrical actuation," *Journal of Applied Physics*, vol. 115, p. 064907, Feb. 2014.
- [36] S.-H. Hwang, H. W. Park, and Y.-B. Park, "Piezoresistive behavior and multi-directional strain sensing ability of carbon nanotubegraphene nanoplatelet hybrid sheets," *Smart Materials and Structures*, vol. 22, p. 015013, Jan. 2013.
- [37] C. Kocabas, N. Pimparkar, O. Yesilyurt, S. J. Kang, M. A. Alam, and J. A. Rogers, "Experimental and theoretical studies of transport through large scale, partially aligned arrays of single-walled carbon nanotubes in thin film type transistors," *Nano Letters*, vol. 7, no. 5, pp. 1195–1202, 2007. PMID: 17394371.
- [38] S. Kumar, J. Y. Murthy, and M. A. Alam, "Percolating conduction in finite nanotube networks," *Phys. Rev. Lett.*, vol. 95, p. 066802, Aug 2005.

- [39] A. Oliva-Avils, F. Avils, G. Seidel, and V. Sosa, "On the contribution of carbon nanotube deformation to piezoresistivity of carbon nanotube/polymer composites," *Composites Part B: Engineering*, vol. 47, pp. 200–206, Apr. 2013.
- [40] B. De Vivo, P. Lamberti, G. Spinelli, V. Tucci, L. Vertuccio, and V. Vittoria, "Simulation and experimental characterization of polymer/carbon nanotubes composites for strain sensor applications," *Journal of Applied Physics*, vol. 116, p. 054307, Aug. 2014.
- [41] R. Rahman and P. Servati, "Effects of inter-tube distance and alignment on tunnelling resistance and strain sensitivity of nanotube/polymer composite films," *Nanotechnology*, vol. 23, p. 055703, Jan. 2012.
- [42] N. Hu, Y. Karube, C. Yan, Z. Masuda, and H. Fukunaga, "Tunneling effect in a polymer/carbon nanotube nanocomposite strain sensor," *Acta Materialia*, vol. 56, pp. 2929–2936, Aug. 2008.
- [43] J. G. Simmons, "Generalized formula for the electric tunnel effect between similar electrodes separated by a thin insulating film," *Journal of Applied Physics*, vol. 34, pp. 1793–1803, June 1963.
- [44] A. Oskouyi, U. Sundararaj, and P. Mertiny, "Tunneling conductivity and piezoresistivity of composites containing randomly dispersed conductive nano-platelets," *Materials*, vol. 7, pp. 2501–2521, Mar. 2014.
- [45] S. Stassi, G. Canavese, F. Cosiansi, R. Gazia, C. Fallauto, S. Corbellini, M. Pirola, and M. Cocuzza, "Smart piezoresistive tunnelling composite for flexible robotic sensing skin," *Smart Materials and Structures*, vol. 22, p. 125039, Nov. 2013.

- [46] W. S. Bao, S. A. Meguid, Z. H. Zhu, and M. J. Meguid, "Modeling electrical conductivities of nanocomposites with aligned carbon nanotubes," *Nanotechnology*, vol. 22, p. 485704, nov 2011.
- [47] W. Fang, H. W. Jang, and S. N. Leung, "Evaluation and modelling of electrically conductive polymer nanocomposites with carbon nanotube networks," *Composites Part B: Engineering*, vol. 83, pp. 184–193, Dec. 2015.
- [48] D. K. Davies, "Charge generation on dielectric surfaces," *Journal of Physics D: Applied Physics*, vol. 2, pp. 1533–1537, nov 1969.
- [49] G. R. Ruschau, S. Yoshikawa, and R. E. Newnham, "Resistivities of conductive composites," *Journal of Applied Physics*, vol. 72, pp. 953–959, Aug. 1992.
- [50] F. Panozzo, M. Zappalorto, and M. Quaresimin, "Analytical model for the prediction of the piezoresistive behavior of CNT modified polymers," *Composites Part B: Engineering*, vol. 109, pp. 53–63, Jan. 2017.
- [51] T. Yasuoka, Y. Shimamura, and A. Todoroki, "Electrical resistance change under strain of CNF/flexible-epoxy composite," *Advanced Composite Materials*, vol. 19, pp. 123–138, Jan. 2010.
- [52] S. Kirkpatrick, "Percolation and conduction," *Rev. Mod. Phys.*, vol. 45, pp. 574–588, Oct 1973.
- [53] O. Kanoun, C. Miller, A. Benchirouf, A. Sanli, T. Dinh, A. Al-Hamry, L. Bu, C. Gerlach, and A. Bouhamed, "Flexible carbon nanotube films for high performance strain sensors," *Sensors*, vol. 14, pp. 10042–10071, June 2014.
- [54] A. P. Chatterjee, "A percolation-based model for the conductivity of nanofiber composites," *The Journal of Chemical Physics*, vol. 139, no. 22, p. 224904, 2013.

- [55] R. Taherian, “Experimental and analytical model for the electrical conductivity of polymer-based nanocomposites,” *Composites Science and Technology*, vol. 123, pp. 17 – 31, 2016.
- [56] A. Behnam and A. Ural, “Computational study of geometry-dependent resistivity scaling in single-walled carbon nanotube films,” *Phys. Rev. B*, vol. 75, p. 125432, Mar 2007.
- [57] B. Hu, N. Hu, Y. Li, K. Akagi, W. Yuan, T. Watanabe, and Y. Cai, “Multi-scale numerical simulations on piezoresistivity of CNT/polymer nanocomposites,” *Nanoscale Research Letters*, vol. 7, no. 1, p. 402, 2012.
- [58] W. S. Bao, S. A. Meguid, Z. H. Zhu, and G. J. Weng, “Tunneling resistance and its effect on the electrical conductivity of carbon nanotube nanocomposites,” *Journal of Applied Physics*, vol. 111, no. 9, p. 093726, 2012.
- [59] X. Ren and G. D. Seidel, “Computational micromechanics modeling of piezoresistivity in carbon nanotubepolymer nanocomposites,” *Composite Interfaces*, vol. 20, pp. 693–720, Dec. 2013.
- [60] T. Tallman and K. W. Wang, “Analytically modeling the piezoresistivity of CNT composites with low-filler aggregation,” in *Sensors and Smart Structures Technologies for Civil, Mechanical, and Aerospace Systems 2013* (J. P. Lynch, C.-B. Yun, and K.-W. Wang, eds.), vol. 8692, pp. 278 – 283, International Society for Optics and Photonics, SPIE, 2013.
- [61] N. A. Mohd Radzuan, A. B. Sulong, and J. Sahari, “A review of electrical conductivity models for conductive polymer composite,” *International Journal of Hydrogen Energy*, vol. 42, pp. 9262–9273, Apr. 2017.
- [62] Y. Zare and K. Y. Rhee, “A simple methodology to predict the tunneling conductivity of polymer/CNT nanocomposites by the roles of tunneling distance, interphase and CNT waviness,” *RSC Advances*, vol. 7, no. 55, pp. 34912–34921, 2017.

- [63] Y. Wang and X. Zhao, "A theoretical model of effective electrical conductivity and piezoresistivity of carbon nanotube composites," *Philosophical Magazine Letters*, vol. 98, pp. 38–43, Jan. 2018.
- [64] J. Ku-Herrera and F. Avils, "Cyclic tension and compression piezoresistivity of carbon nanotube/vinyl ester composites in the elastic and plastic regimes," *Carbon*, vol. 50, pp. 2592–2598, June 2012.
- [65] J. Leng and A. K. T. Lau, *Multifunctional polymer nanocomposites*. CRC Press, 2011.
- [66] "Applied sciences, inc. pyrograf iii." www.apsci.com.
- [67] "Smooth on, inc. ecoflex 00-30." <https://www.smooth-on.com/products/ecoflex-00-30/>.
- [68] ASTM F84-99, "Standard test method for measuring resistivity of silicon wafers with an in-line four-point probe," standard, ASTM International, West Conshohocken, PA, 2002.
- [69] X. Ni, C. Hui, N. Su, W. Jiang, and F. Liu, "Monte carlo simulations of electrical percolation in multicomponent thin films with nanofillers," *Nanotechnology*, vol. 29, p. 075401, jan 2018.
- [70] S. Shang, L. Gan, M. C.-w. Yuen, S.-x. Jiang, and N. Mei Luo, "Carbon nanotubes based high temperature vulcanized silicone rubber nanocomposite with excellent elasticity and electrical properties," *Composites Part A: Applied Science and Manufacturing*, vol. 66, pp. 135–141, Nov. 2014.
- [71] T. Giffney, E. Bejanin, A. S. Kurian, J. Travas-Sejdic, and K. Aw, "Highly stretchable printed strain sensors using multi-walled carbon nanotube/silicone rubber composites," *Sensors and Actuators A: Physical*, vol. 259, pp. 44–49, June 2017.

- [72] P. Wang, S. Geng, and T. Ding, “Effects of carboxyl radical on electrical resistance of multi-walled carbon nanotube filled silicone rubber composite under pressure,” *Composites Science and Technology*, vol. 70, pp. 1571–1573, Sept. 2010.
- [73] S. Gong and Z. H. Zhu, “On the mechanism of piezoresistivity of carbon nanotube polymer composites,” *Polymer*, vol. 55, pp. 4136–4149, Aug. 2014.